DENSITY CONTRAST SHELL MODELS FOR THE PLANETARY NEBULA IC 2165

S. HYUNG

Department of Astronomy, University of California, Los Angeles, CA 90024
Received 1992 September 28; accepted 1993 June 21

ABSTRACT

Since planetary nebulae are spatially extended sources, measurements of individual line fluxes may pertain to different areas of their images. Photoelectric or infrared observations of the strongest lines may embrace the entire image; *International Ultraviolet Explorer* observations involve an elliptical aperture, $10'' \times 23''$; while a spectrum scanner or slit spectrograph takes a narrow *pencil,* typically $\sim 2'' \times 4''$, through a selected portion of the nebula. Therefore, we should be able to use a theoretical model to predict the emission from any one of these traverses, provided that the observers describe accurately the regions they have selected. Thus the present investigation involves not just the calculation of models, hopefully improved by including the best available physics, radiative transfer, charge-exchange and atomic data, etc., but also the development of procedures for predicting the emission from cross sections of arbitrary placement, shape, and size, taken thru the nebular image. Spherically symmetrical shells pose no great difficulty, but most regularly shaped planetary nebulae show a bilateral symmetry. Since the axis of symmetry can be oriented at any angle with respect to the plane of the sky, calculations of the flux from a pencil beam now become more intricate, since a ray may pass through zones of quite different density.

Detailed results are presented for the well-observed high-excitation planetary nebula IC 2165, for which observations with different techniques and pencils of varying size have been obtained. By comparing each body of observational data with its appropriate theoretical nebular slice, it is believed that substantially improved chemical compositions are found; model abundances, log N on the scale log $N(\mathrm{H}) = 12.00$, are He = 11.02, C = 8.61, N = 7.90, O = 8.30, Ne = 7.70, Si = 6.48; S = 6.45, Cl = 4.95, Ar = 6.00, K = 4.90, Ca = 5.08.

Subject headings: ISM: abundances — planetary nebulae:general — planetary nebulae: individual (IC 2165)

1. INTRODUCTION

The evolutionary role of planetary nebulae (PNs) has been reviewed by many authors, e.g., Kwok (1982), Balick (1987) and at IAU Symposium 155, Planetary Nebulae (Innsbruck). One of our objectives is to get abundances of chemical elements in ejecta in order to cast light on nucleogenesis in the last stage of evolution of the progenitor star and to estimate the consequent enrichment of the He, C, N, and O contents of the interstellar medium (ISM).

The problem of the chemical analysis of PNs is very much more difficult than the analysis of a stellar atmosphere, for a number of reasons: A star appears as a point source which has a unique spectrum, while a PN displays an extended surface whose spectrum may vary with distance and position angle from the planetary nebula nucleus (PNN). A stellar atmosphere is often near thermodynamic equilibrium, so that if we observe an element in one stage of ionization, with a good model atmosphere we can calculate accurately the numbers of atoms in all other stages of ionization. No such luxury is available for a PN. For a star, one needs only the energy distribution in the spectrum, the shape or profiles of certain strong lines, and the "total intensities" or equivalent widths of others. The situation is far different for a PN because it has an extended surface. One needs monochromatic images for the stronger lines such as the H and He recombination lines, and collisionally excited [O III], [O II], [N II], etc.

To exacerbate our difficulties, PNs are not spherically symmetrical; even under the most favorable circumstances they exhibit at best only a bilateral symmetry with initially unknown orientation of axes and dependence of the shell thickness on latitude. Furthermore, the spectroscopic observations themselves often refer to different quantities. Some include radiation from the entire nebular image but pertain only to stronger lines. Others involve slit spectroscopic data obtained over only a limited area of the image but reaching precious lines of many elements needed for diagnostics and abundance studies.

1. Conventional photoelectric spectrophotometry can yield the total fluxes for strong lines in nebulae of small angular size, but it throws away all the structural information, since it integrates over the entire PN image.

2. Likewise, infrared measurements often cover the entire image of small or medium-sized nebula.

3. The oval aperture, $10'' \times 23''$, of the *International Ultraviolet Explorer* (*IUE*) may accommodate the entire image of a small PN, but with an extended object such as NGC 7009 one needs to make settings in known positions (Barker 1983) and utilize isophotic contours.

4. The image dissector scanner (IDS) enables spectral measurements to be made from 3200 to 8500 Å with typical slot sizes $2'' \times 4''$ or $2'' \times 6''$. The great advantage of this system is that sky subtraction is possible.

5. Slit spectroscopy typically uses a narrow ($\sim 1''$–$2''$) slit of several arcseconds length. Spectral resolution is vastly superior to that obtainable with a spectral scanner or IDS system. The Hamilton echelle spectrograph on the Lick 3 m Shane tele-

y

scope combines the advantages of a charge-coupled device (CCD) detector—which yields a linear response—with the high spectral resolution of the coudé spectrograph. Data obtained with this instrument provide the backbone of the present investigation, although data from other sources are also considered.

Section 2 reviews briefly some aspects of previous models which are related to the current study. I also explain why a three-dimensional calculation entails difficulties because of a very complicated radiative transfer problem. Section 3 describes the data acquisition system used in the Hamilton echelle spectrograph and compiles pertinent data from different available sources. The Hamilton echelle and *IUE* data are analyzed to get nebular diagnostics. Section 4 recalls the relevant nebular physics and the equilibrium equations for a model planetary nebula. The diffuse ionizing radiation is also discussed in § 4. In § 5, I further describe some numerical aspects of this study, particularly the method of constructing model geometry and the radiative transfer problem. The role of dust also has been included in the program, and a description of its influence is presented in § 6. In § 7, I apply the model calculation procedures to the nebula IC 2165 and discuss the results. Finally, concluding remarks are given in § 8.

2. SOME COMMENTS ON IONIZATION MODELS

Theoretical models as tools for assessing observations of symmetrical (though not necessarily spherically symmetrical) PNs are generally of two types: rather approximate models used as tools for handling large bodies of data and precise, rather elaborate models tailored to individual objects. Helpful general remarks on ionization models are to be found in Harrington (1983, 1989) and Péquignot (1983).

In the context of the approximate model approach we mention that of Keyes & Aller (1978), based on a procedure originally due to B. Balick and applied by Aller & Czyzak (1983), Aller et al. (1987), and Aller & Keyes (1987). Somewhat improved calculations of this type have been made for Magellanic Cloud PNs by Dopita & Meatheringham (1990), who derived a composite program for automatic ionization modeling and applied it to southern PNs.

In all of these methods the parameters that are varied to fit the observed nebular spectrum include (1) the chemical composition, (2) the density and its variation with distance from the central star, and (3) the energy distribution in the PNN spectrum. In many investigations, the PNN flux is assumed to be Planckian or has been based on model atmosphere calculations. Sometimes arbitrary or ad hoc modifications have been adopted for high-temperature PNNs. The model calculations sometimes have to be truncated within the full Strömgren sphere in order to reproduce the observed spectra reasonably well. That is, such models are material-limited.

The Balick program as modified by Keyes appears to work well for nebulae of low to moderate excitation but is less successful for high-excitation objects. Here, for example, one should use radiative transfer theory rather than the on-the-spot (OTS) approximation.

When good observational data are available for symmetrical PNs, detailed modeling taking the geometry into account appears to be worthwhile. Examples include NGC 7662 and IC

3568 modeled by Harrington et al. (1982) and Harrington & Feibelman (1983) and NGC 3918 modeled by Clegg et al. (1987).

As has already been suggested by a number of investigators (e.g., Balick 1987), the nonspherically symmetrical appearance of PNs in the sky might be due to a density contrast between the equatorial and the polar regions. To model NGC 3918, Clegg et al. (1987) and Harrington, Monk, & Clegg (1988) adopted a cone and toroidal ring structure with densities differing by a factor of 3 in the two regions. Models are calculated for each region and weighted according to the emitting volumes involved.

Theoreticians present fluxes integrated over the entire radiating volume of a model nebula. The predictions are then compared with observed data, only some of which may refer to radiation emitted from the entire image. In practice, nearly all data obtained with a slit spectrograph or ITS pertain to a small column taken through the nebular image. For example, observations obtained with the Hamilton echelle spectrograph all refer to a small rectangular cross section through the nebula (in our program amounting to $\simeq 1\rlap{.}''16 \times 4\rlap{.}''0$) and not to its total radiation. Thus, since observations are made not over the entire PN image but at a particular small area of it, we should incorporate the corresponding slot size and its placement in the nebular program. This refinement can have an enormous influence on the predicted spectrum.

For a spherically symmetrical nebula where all the properties depend only on the radius, the procedure is relatively simple. The predicted surface brightness can be compared only with observations averaged over all position angles and can give only a rough approximation for most PNs.

The present program is aimed at bilaterally symmetrical nebulae in which the density and/or thickness of the radiating volume depends only on the colatitude θ_0 and not on the azimuthal (longitude) angle ψ_0. The program endeavors to include the best available physics, e.g., radiative transfer considerations are included rather than the OTS approximation. Effects of dust are also recognized. We approximate the actual structures of the more regular planetary nebulae, with equatorial toroidal rings plus polar cones of reduced densities. In this way these models resemble those of Clegg et al. (1987), for example. However, I will not simply add two different model calculations to get a composite model. This procedure may work well for calculating an integrated spectrum. It is not adequate for our present problem. Instead, I will introduce a three-dimensional grid space and obtain the corresponding surface brightness and line intensities in the proposed PN geometry. Thus, in the proposed modeling procedures, not only the line spectra of the nebula but also its geometrical structure will be carefully treated. To accomplish the objective of constructing more reliable three-dimensional models, it is also desirable to solve the radiative transfer problem between two shells of different density (see § 5). Thus, the unique character of the present investigation is not simply to construct models for additional planetary nebulae but rather to develop techniques for comparing model predictions with actual telescopic observations, i.e., the observed line fluxes as obtained either in integrated light or from pencils of arbitrary size taken through the nebular image, with due regard to the overall nebular morphology.

3. OBSERVATIONAL DATA

Clearly, we need infrared (IR), ultraviolet (UV), and radio-frequency (rf) data as well as optical region observations to investigate a nebula properly. Fortunately, a fair number of such data are available for our target object IC 2165.

3.1. Instrumentation and Calibration Data for Hamilton Spectrograph

Our PN observations have all been made with the Shane 3 m telescope at Lick Observatory and with the Hamilton echelle spectrograph. Measurements of IC 2165 are part of a much more extensive series of PN observations. In order to achieve the best match with a CCD detector such as the TI 800×800 chip presently used in this equipment, the Hamilton spectrograph features an echelle grating with about 316 grooves cm^{-1}. To obtain high spectral resolution, large optical elements are required, in this instance a 20 cm beam with gratings, Schmidt corrector lens, and camera to match. A pair of prisms is placed in the beam to separate the orders. In the wavelength range 3600–10300 Å, one works with the 60th to 160th orders. The spectrum consists of a sequence of nearly parallel, clipped sections well suited in arrangement for a CCD detector chip.

The extent of the spectrum greatly exceeds the area of the CCD chip, so that in order to cover the spectrum, about six different chip positions are required (see Table 1). There is some overlap, so that some check on the photometry is provided. To cover the region 3650–4700 Å, one chip setting, denoted setup 121, sufficed, but as we go to longer wavelengths, each spectral segment lengthens and successive strips fall closer together. Thus for the region 4300–6300 Å, two CCD chip settings denoted setups 122 and 123 were required, while for the region 5300–10300 Å, three chip settings, setups 124, 125, and 126, are required. One chip setting, setup "127," was chosen to obtain the important lines Hα, Hβ, [N λ6548, He I λ5876, [O III] λ4959, and [O III] λ5007 in one exposure.

The great intensity range between the strongest and weakest lines poses a severe problem. To measure the relatively weak lines, longer dwell times are needed for each wavelength setting to reduce the noise-to-signal ratio. On the other hand, some of the strongest lines are easily saturated and *bleed* into other nearby orders in those longer exposures. To avoid saturation and bleeding effects in the CCD detector, a relatively short dwell time is also required for some settings which contain strong lines. Required exposures in the violet are invariably long (over 1 hr). Although the detailed integration time varies for each PN, exposure times of 1–20 minutes for the strong lines and 1–2 hr for the weak lines were used in the observing runs. Thus we take a slit width of 640 μm (1″16 on the sky) and a length of 4″0 as most practical; a slit length much longer than 4″0 would cause echelle orders to overlap, while a shorter slit length would admit too little light.

In order to establish the response function of the equipment, including evaluation of the echelle blaze function, we need comparison star observations. Also, flat-field and dark readings are required.

Standard (comparison) stars.—Bright naked-eye stars 58 Aql (A type, $m_v = 5.53$) and υ Ori (B type, $m_v = 4.63$) observed with a wide (4″0) slit to eliminate atmospheric dispersion effects served as spectrophotometric standards; typical exposures were about 240 and 180 s, respectively. For some particular wavelength regions such as Hα and Hβ, we must carefully interpolate over the absorption-line profiles. For the violet region setting denoted setup 121, we used BD + 28°4211, which has weak Balmer lines, since the spectra of 58 Aql or υ Ori are severely impacted by strong Balmer lines shortward of about 3900 Å.

The wavelength was calibrated with exposures on a Th-Ar arc. Flat-field exposures obtained with a bright dome quartz light enabled us to correct for small-scale variations in the response of CCD pixels. Also, exposures secured with no illumination of the chip at all were obtained to subtract readout noise and dark counts from the images.

3.2. Observations and Data Reduction

Table 1 gives the log of the IC 2165 observations. The CCD 2048×2040 chip covers the entire echelle field, but its performance was so inadequate that no data obtained with this chip have been used in the analysis. Typical seeing was about 2″, but on some occasions it was better than 1″. The 1988 December observation was hindered by clouds.

I used the National Optical Astronomy Observatories (1987) IRAF echelle package program (version 2.9) to extract nebular spectral lines from raw images, employing thorium-argon maps (Latham & Sternberg 1977; Palmer & Engeleman 1983) to identify lines. Note that toward the red, where the prismatic dispersion is lower, the spectral strips tend to be jammed closer together. The spectral resolution increases as wavelength decreases; for example, ~ 0.0294 Å pixel^{-1} [23.5 Å (800 pixels)$^{-1}$] at 3600 Å and ~ 0.0743 Å pixel^{-1} [59.5 Å (800 pixels)$^{-1}$] at 8850 Å, respectively.

The spectral energy distribution information provided by the IRAF package had to be supplemented by data for $\lambda > 8400$ Å from Hayes (1970) for 58 Aql and from Code (1960) for υ Ori with the correction factors provided by Hayes & Latham (1975). Uncertainties arise from errors in the adopted stellar energy distribution. The stellar energy distribution was

TABLE 1
OBSERVATIONS FOR IC 2165

Position Setup	Exposure (minutes)	Observation Date (UT)
CCD 800 × 800 121	60	1986 Nov 26
CCD 800 × 800 122	55	1986 Nov 26
CCD 800 × 800 123	55	1986 Nov 26
CCD 800 × 800 124	60	1988 Oct 2
CCD 800 × 800 125	1	1988 Oct 1
CCD 800 × 800 125	10	1988 Oct 1
CCD 800 × 800 125	60	1988 Oct 1
CCD 800 × 800 126	60	1988 Oct 2
CCD 800 × 800 121	33	1988 Dec 18
CCD 800 × 800 121	27	1988 Dec 18
CCD 800 × 800 121	5	1988 Dec 18
CCD 800 × 800 122	90	1989 Nov 17
CCD 800 × 800 123	90	1989 Nov 17
CCD 800 × 800 127	90	1990 Nov 8
CCD 800 × 800 127	5	1990 Nov 8
CCD 2048 × 2048	90	1990 Dec 26
CCD 2048 × 2048	40	1990 Dec 26
CCD 2048 × 2048	5	1990 Dec 26

measured at an insufficient number of points for analyzing the high-resolution echelle spectra. Therefore, we have to interpolate between observed points in the energy distribution, and some uncertainty in the response function can arise from this cause.

First, CCD chip defects and cosmic-ray hits were removed. Then the individual scans of companion star and nebula were divided by the flat field and wavelength corrected by the Th-Ar arc exposures. The comparison star and nebular data are corrected for atmospheric extinction; next, from a comparison of known stellar energy distributions with the corrected stellar scans, we deduce the response function for each order and finally the nebular line fluxes.

Several effects can cause observational errors. The *"bleeding" effect* which impacts other lines in nearby orders from strongly overexposed [O III], [N II], or Hα images usually can be assessed, and contaminated line images corrected when the drip or bleeding effect extends over several orders. All saturated line data are discarded. Since our observations necessarily were carried out sometimes on nights with some moonlight, an absolutely clear sky is required.

The observer attempts to guide, upon the same position of the nebular image, but the image rotates on the slit through a small position angle during the exposure: The effect of image rotation and guiding errors is that a rectangular pencil through the nebula becomes blurred or fuzzy. Thus, it is too restrictive to assume a pencil of $1.''16 \times 4.''0$, not only because of slit rotation but also because of inevitable guiding limitations, since the image often "bounces around" because of seeing fluctuations during an exposure. I estimate that under normal conditions the total blurring can be taken as about $2'' - 3''$. Atmospheric dispersion does not seem to be important for IC 2165, and uncertainties in the different atmospheric corrections between comparison star and nebula does not seem to affect seriously the derived fluxes.

Finally, data from different chip settings have to be combined. We obtain the scaling factors from the overlapping sections between different setup *positions* by using a least-squares method. After carefully rescaling the fluxes relative to the blue region setting (*position* 121) with the aid of appropriate normalization factors, I have averaged the flux from all different exposure data to form one definitive list.

3.3. *The Spectrum of IC 2165 as Measured by the Hamilton Echelle*

Table 2 summarizes the line intensity data for IC 2165. Column (1) gives the observed wavelength, column (2) the identification, column (3) the flux F (Ham) as measured via the Hamilton spectrograph not yet corrected for interstellar extinction on the scale of F (Hβ) = 100, and the formal root mean square (rms) percent error as deduced from internal agreement of measurements made with different chip settings.

To determine interstellar extinction, we may compare certain theoretical flux ratios presumably known under nebular conditions with measured values of the same. We can use (1) the Balmer lines, e.g., $F(\text{H}\alpha)/F(\text{H}\beta)$, $F(\text{H}\gamma)/F(\text{H}\beta)$, which cover only a relatively small wavelength range but are accurately measured, and (2) the Paschen-to-Balmer line ratios, which cover a wider wavelength range, e.g., $F(\text{Pa}n)/F(\text{H}\beta)$ or

$F(\text{Pa}n)/F(\text{Balmer } n)$. For all these ratios the theoretical intrinsic values were taken from Hummer & Storey (1987), calculated for $T_\epsilon = 10,000$ K, $N_\epsilon = 10,000$ cm^{-3}, since all these ratios of recombination-line fluxes depend only very weakly on the temperature and density, at least over the range with which we are concerned. The calculations were carried out using the Seaton (1979) extinction function (k_λ). For each line we derive the value of $C = \log [I(\text{H}\beta)/F(\text{H}\beta)]$, where $F(\text{H}\beta)$ is the value of the Hβ flux deduced from the given H line, and $I(\text{H}\beta)$ is the intensity of Hβ corrected for interstellar absorption. In other words, C is the logarithmic extinction coefficient for Hβ as derived from each line. The resulting coefficients derived from the Paschen lines turn out to be somewhat smaller than those derived from the Balmer line ratios. The reason for this discrepancy appears to be that all the Paschen lines may be systematically affected by a bad response function in this region (probably due to errors in the adopted energy distribution for the comparison stars see § 3.2). I also derived C-values for $T_\epsilon = 15,000$ K, $N_\epsilon = 4000$ cm^{-3} (values chosen from the plasma diagnostics; see Fig. 1); these turn out to be slightly higher. I finally adopted a value of $C \sim 0.68$ (Hα/Hβ and Hδ/Hβ) from method (1) above to correct optical fluxes for interstellar extinction.

Columns (6), (7), (8), and (9) of Table 2 compile data from five spectrophotometric studies of IC 2165 all corrected for interstellar extinction. The reddening function, $f(\lambda)$, $[f(\lambda) = 0$ at Hβ λ4861] is derived from Seaton (1979) and is presented in column (5). For λ < 3200 Å (Table 2A), column (6) gives the *IUE* data based on Marionni & Harrington's (1981) measurements, and in column (9) from my own rediscussion. The *IUE* satellite spectra were taken with the large entrance aperture (10″ × 23″ oval), low-dispersion format, using both the long-wavelength redundant (LWR) and shortwavelength prime (SWP) cameras. I have remeasured the fluxes from LWR 10217L, LWR 7430L, LWR 2255L, SWP 8678L, and SWP 2461L that were supplied by the National Space Science Data Center (NSSDC) with a new data reduction system. As above, the observed fluxes, $F(\lambda)$, have been corrected for interstellar extinction ($C = 0.68$, $E_{B-V} = 0.463$) with the Seaton $f(\lambda)$ to obtain $I(\lambda)$ based on the scale of $I(\text{H}\beta) = 100$. The intensity ratio $F(\text{He II } \lambda4686)/F(\text{He II } \lambda1640)$ is adopted from the determination of Marionni & Harrington (1981).

For the 3620–10200 Å range (Table 2B), column (6) gives intensities derived from our Hamilton echelle data. Column (7) lists the ITS data obtained at Lick Observatory in the 3600–8500 Å range. The extinction coefficient applied here in this column is $C = 0.62$ (Aller & Czyzak 1983, 1979). Since the slot used in the ITS observations (2″ × 4″ or 2″ × 6″) is close to the *effective* pencil size [$\sim (2''-3'') \times 4''$] of the Hamilton echelle observations, the spectrum in column (7) is comparable to that listed in column (6). Because of the relatively poor spectral resolution of the ITS, some lines such as λλ7319, 7330, λλ3967, 3970, and λλ3726, 3729 are unresolved. Some line ratios such as [O II] λ3726/λ3729, however, might be separated empirically by invoking slit spectra results. Both the Hamilton echelle and the ITS spectra represent the emissions from the central portion of IC 2165.

In column (8) the results of slit photographic spectrophotometry in the 3100–5000 Å range are presented from Kaler,

TABLE 2A
SPECTRUM OF IC 2165: 1240 Å $\leq \lambda \leq$ 3415.65 Å

λ(Å)	Identification	F(Ham)	RMS	f(λ)	I*(IUE)	I(ITS)	I(ptg)	I(IUE)
1240.00	N V 1240			1.639	47.07			71.79
1400.00	[O IV]SiIV 1400			1.307	39.65			44.09
1487.00	[N IV] 1487			1.229	47.42			32.53
1549.00	C IV 1549			1.184	975.23			1030.91
1575.00	[Ne V] 1575			1.168				16.32
1602.00	[Ne IV] 1602			1.153				11.64
1640.00	He II 1640			1.136	260.07			260.07
1664.00	[O III] 1664			1.128	32.98			30.46
1751.00	[N III] 1751			1.120	36.97			32.82
1887.00	[Si III]1887			1.200	3.22			9.29
1907.00	[C III] 1907			1.226	853.05			
1909.00	[C III] 1909			1.229	836.62			943.17
2328.00	[C II] 2328			1.349	82.66			77.98
2422.00	[Ne IV] 2422			1.120	109.83			111.51
2512.00	He II 2512			0.953	11.78			13.57
2734.00	He II 2734			0.700	10.57			16.39
2784.00	[Mg V] 2784			0.659	4.98			7.70
2800.00	Mg II 2800			0.646	6.12			3.66
2837.00	O III 2837			0.619	8.68			14.43
3028.00	3028			0.504				6.52
3048.00	O III 3048			0.494	8.00			14.13
3121.90	O III 3121.7			0.459		1.45	11.30	
3132.73	O III 3132.9			0.454		125.89	98.80	
3187.35	He I 3187.7			0.431		6.17	5.04	
3204.00	He II 3204			0.424		17.38	14.20	
3234.00	S III 3234.0			0.412		0.74	0.62	
3241.70	[Na IV] 3241.7			0.409		0.39	0.32	
3256.60	3256.6			0.403			0.44	
3265.70	O III 3265.4			0.400		0.83	0.71	
3294.10	3294.1			0.389			0.19	
3299.55	O III 3299.4			0.387		3.72	3.18	
3312.15	O III 3312.3			0.382		8.13	6.91	
3323.80	S III 3323.8			0.378		0.32	0.28	
3340.35	O III 3340.7			0.372		10.23	8.87	
3342.70	[Ne III]/[Cl III]			0.372		20.42		
3345.95	[Ne V] 3345.8			0.370		0.65	17.90	
3369.20	3369.2			0.362			0.56	
3385.45	O IV 3385.5			0.357		0.31	0.27	
3407.20	O II 3407.4			0.350		0.72	0.65	
3415.65	O III 3415.3			0.347		2.00	1.80	

Czyzak, & Aller (hereafter KCA). Since a narrow slit is used both here and in the Hamilton system; we call this column of slit data "ptg" to indicate photographic photometry. Since the narrow ($\simeq 1''$ or $\simeq 2''$) slit used in these measurements extends out to the nebular outer boundary, the line emission in the slit ptg spectra corresponds to something between the Hamilton/ ITS, on the one hand, and photoelectric, on the other, but closer to the former. Photoelectric spectrophotometry of emission lines is presented in column (9) (Torres-Peimbert & Peimbert 1977, hereafter TPP, for 7400 Å > λ > 3400 Å; KCA). The resolution is about 16–18 Å for the *red* setting and 8–9 Å for the *blue* setting. Because of the poor resolution of the system, $\lambda 6717/\lambda 6731$ and $\lambda\lambda 6548$, 6563, 6584 were partly blended; the line intensities of these individual lines were estimated by deconvolution of the line blends. The extinction coefficient found and applied here is $C = 0.5$ (TPP). We have only the strongest lines in the photoelectric scanner observation. Because of the large area of the entrance aperture the line emissions in this column are summed over the whole nebula.

The disparity of extinction coefficients used in reductions of the various flux measurements could be attributed to errors in measured fluxes or to a possible scaling error in the flux calibration. The discrepancy in extinction coefficients does not actually influence our further discussions and conclusions, since the line ratios, which will determine the plasma diagnostics, are obtained from a relatively narrow wavelength range.

3.4. Plasma Diagnostics and Ionic Concentrations

Conventional procedures have been employed to obtain the plasma diagnostics from the measured fluxes, corrected for interstellar extinction as described above. The necessary data and essential methods are found, for example, in Aller (1984, 1990) and Osterbrock (1989). Certain line ratios, e.g., [O III] ($\lambda 4959 + \lambda 5007$)/$\lambda 4363$, depend almost entirely on the electron temperature T_e at nebular densities, while $\lambda 6583/\lambda 5755$ of [N II] shows more sensitivity to the electron density; [O II] $\lambda 3726/\lambda 3729$ and [Ar IV] $\lambda 4711/\lambda 4740$ depend strongly on the electron density, while the auroral/nebular ratios in p^3 configurations, e.g., [O II] $\lambda 3727/(\lambda 7320 + \lambda 7330)$, depend

TABLE 2B

SPECTRUM OF IC 2165: 3426.13 Å ≤ λ ≤ 10123.23 Å

λ(Å)	Identification	F(Ham)	RMS	f(λ)	I(Ham)	I(ITS)	I(ptg)	I(P.E.)
3426.13	[Ne V] 3425.9			0.343		58.88	35.20	(28*)
3429.00	O III 3428.7			0.343		3.98	3.70	
3444.03	O III 3444.1			0.338		17.78	16.30	(13*)
3448.00	He I 3447.6			0.336		0.49	0.44	
3554.40	He I 3554.4			0.304		0.42		
3560.10	O IV 3560			0.303			0.40	
3587.30	He I 3587.3			0.295		0.26	0.25	
3634.40	He I 3634.2			0.282		0.48	0.47	
3676.39	H I (B 22) 3676.36	0.61		0.270	0.93	0.60	0.74	
3679.67	H I (B 21) 3679.35	0.56		0.270	0.86	0.66	0.80	
3683.15	H I (B 20) 3682.81	0.69		0.269	1.04	0.71	0.86	
3687.07	H I (B 19) 3686.83	0.82		0.268	1.25	0.83	0.99	
3691.68	H I (B 18) 3691.56	0.80		0.266	1.22	0.95	1.14	
3697.51	H I (B 17) 3697.15	0.83		0.265	1.26	1.20	1.46	
3704.03	H I (B 16) 3703.86	1.02		0.272	1.55	1.17	1.20	
3705.22	He I 3705.02	0.54		0.271	0.82	1.26	1.27	
3712.13	H I (B 15) 3711.97	1.05		0.269	1.61	1.78	1.80	
3722.00	H I (B 14)/[S III]	1.87		0.267	2.85	2.75	2.81	
3726.18	[O II] 3726.03	12.14		0.266	18.39	22.39	22.90	
3728.96	[O II] 3728.82	6.18		0.265	9.36	13.80	14.00	56.20
3734.60	H I (B 13) 3734.37	1.96		0.263	2.96	2.45	2.53	
3750.29	H I (B 12) 3750.15	2.31		0.259	3.47	3.09	3.03	
3754.87	O III 3754.67	0.65		0.258	0.98	0.76	1.06	
3757.55	N III 3757.60	0.35		0.257	0.53	0.24	0.29	
3760.07	O III+? 3759.81	2.77		0.256	4.14	3.31	3.89	
3770.77	H I (B 11) 3770.63	2.57		0.253	3.82	4.17	3.66	
3774.00	O III/[Fe IV]			0.253			0.23	
3782.40	He II 3782.4			0.250			0.20	
3791.64	O III? 3791.26	0.34		0.248	0.50		0.19	
3798.04	H I (B 10) 3797.90	3.67		0.246	5.40	5.01	4.97	
3814.10	He II 3814.1			0.242			0.25	
3819.92	He I 3819.61	0.61		0.240	0.89	0.76	1.07	
3827.80	3827.8			0.238			0.10	
3833.96	He I 3833.57	0.37		0.237	0.54		0.38	
3835.57	H I (B 9) 3835.39	5.08		0.236	7.36	7.24	6.67	
3843.00	O II 3843+?	0.51		0.235	0.74			
3854.62	Si II 3856?	0.17		0.232	0.25			
3858.20	He II 3858.1	0.30		0.231	0.44		0.32	
3862.86	Si II 3862.59	0.38		0.229	0.54			
3868.91	[Ne III] 3868.71	60.00	1%	0.228	85.70	95.50	79.60	100.0

λ(Å)	Identification	F(Ham)	RMS	f(λ)	I(Ham)	I(ITS)	I(ptg)	I(P.E.)
3887.66	He II 3887.4	0.33		0.223	0.47			
3889.09	H I (B 8) 3889.05	12.56		0.223	17.80	20.42	15.70	
3895.86	[Fe V] 3895.5	0.38		0.221	0.53			
3905.20	Si I 3905.3			0.219			0.07	
3908.40	3908.4			0.218			0.06	
3923.66	He II 3923.5	0.37		0.214	0.52	0.81	0.57	
3938.40	3938.4			0.211			0.07	
3945.40	O II 3945.05			0.209			0.06	
3951.70	3951.7			0.207			0.04	
3964.87	He I 3964.73	0.31		0.204	0.43		0.47	
3967.62	[Ne III] 3967.41	18.81	1%	0.203	25.84	28.18	18.30	(18*)
3968.75	He II 3968.5	0.30		0.203	0.41			
3970.25	H I (B 7) 3970.07	9.80	5%	0.203	13.46	15.85	18.10	
3996.20	O IV/[F IV] 3996.2			0.197			0.15	
4010.40	He I 4010.4			0.193			0.19	
4026.23	He I/He II 4026.3	1.54		0.189	2.07	1.70	2.74	
4046.00	4046.0			0.185			0.11	
4051.20	4051.2			0.184			0.12	
4068.81	[S II] 4068.60	0.65		0.180	0.87	2.29	2.26	
4070.48	C III 4070.2	0.29		0.179	0.39			
4072.52	O II 4072.16	0.45		0.179	0.60			
4074.51	O III 4074?	0.22		0.178	0.29			
4076.62	[S II] 4076.35	0.54		0.178	0.71		0.80	
4085.90	4085.9			0.176			0.12	
4097.51	N III 4097.31	1.32		0.173	1.74	1.51	1.51	
4100.23	He II 4100.0	0.80		0.172	1.05			
4101.90	H I (δ) 4101.76	19.70	2%	0.172	25.76	26.92	23.80	26.92
4103.57	N III 4103.37	0.62		0.172	0.81		0.43	
4120.68	He I 4120.81			0.168			0.13	
4121.12	He I/O II 4121	0.16		0.168	0.20	0.30	0.27	
4129.30	O II 4129.3			0.166			0.09	
4143.98	O II 4143.77	0.26		0.163	0.34	0.15	0.45	
4156.00	O II/C III 4156.0			0.160			0.08	
4163.39	[K V] 4163.90	0.11		0.158	0.14		0.10	
4169.32	He I 4168.97	0.08		0.157	0.10		0.07	
4187.03	C III 4186.8	0.17		0.154	0.21	0.23	0.36	
4196.04	N III 4195.6	0.06		0.153	0.08			
4200.01	He II 4199.83	0.78	29%	0.152	0.99	1.17	1.22	
4227.76	[Fe V] 4227.5	0.24		0.147	0.31	0.29	0.26	
4267.38	C II 4267.18	0.27	1%	0.141	0.33	0.41	0.46	

124

TABLE 2B—Continued

λ(Å)	Identification	F(Ham)	RMS	f(λ)	I(Ham)	I(ITS)	I(ptg)	I(P.E.)
4314.30	C II 4314.5			0.133			0.06	
4338.89	He II 4338.67	1.15	11%	0.129	1.41			
4340.67	H I (γ) +?	44.98	5%	0.129	55.03	46.77		46.77
4363.41	[O III] 4363.21	17.09	1%	0.123	20.75	19.05	22.80	21.38
4369.00	4369.0			0.122			0.10	
4379.24	N III 4379.09	0.10	14%	0.119	0.12		0.12	
4388.16	He I 4387.93	0.29	4%	0.117	0.35		0.75	
4396.50	O II 4396.0			0.115		0.28	0.14	
4415.53	OII 4417.1?	0.07		0.110	0.09			
4437.26	He I 4437.55	0.09		0.104	0.11			
4448.10	O II? 4448.21			0.101			0.06	
4453.13	O II 4452.4	0.06	2%	0.100	0.07		0.07	
4471.72	He I 4471.50	2.42	5%	0.095	2.81	2.51	4.70	4.79
4505.96	line?	0.52		0.086	0.59			
4511.30	[K IV]/[K IV] 4511	0.16		0.085	0.18			
4534.78	N III 4534.57	0.06		0.079	0.07			
4541.82	He II 4541.59	1.73	8%	0.077	1.96	1.91	2.56	
4562.60	[Mg I] 4562	0.11	35%	0.072	0.13		0.08	
4571.15	Mg I 4571.00	0.19	10%	0.070	0.21		0.58	
4575.00	4575.0			0.069			0.18	
4606.51	[Fe III] 4607.1?	0.08	6%	0.061	0.08			
4608.00	O II 4609.4?			0.061			0.29	
4631.96		0.10		0.055	0.11			
4634.23	N III 4634.16	1.10	7%	0.054	1.19	1.15	1.65	
4640.64	N III 4640.64	1.96	10%	0.053	2.13	2.34	3.46	
4641.95	N III 4641.90	0.28	8%	0.052	0.31			
4647.69	C III+? 4647.40	0.34		0.051	0.37			
4649.26	O II 4649.14	0.10		0.051	0.11			
4650.50	O II 4650.84	0.15		0.050	0.16	0.54	0.75	
4651.63	C III 4651.35	0.09		0.050	0.10			
4655.60	4655.6			0.049		0.51		
4657.70	[Fe III] 4658.10	0.16	4%	0.049	0.17			
4658.57	C IV 4658.64	0.40	6%	0.049	0.43			
4685.79	He II 4685.68	59.39	15%	0.042	63.48	61.66	0.58	41.60
4701.09	[Fe III] 4701.62	0.09		0.038	0.10			
4702.29	[FeII] 4701.3?	0.04		0.038	0.04			
4711.42	[Ar IV] 4711.34	5.04	12%	0.036	5.33	7.08	7.63	
4713.21	He I 4713.14	0.53	2%	0.036	0.57			
4714.34	[Ne IV] 4714.25	0.64	18%	0.035	0.68			
4715.82	[Ne IV] 4715.61	0.21	25%	0.035	0.22			
4724.36	[Ne IV]+? 4724.15	0.65	21%	0.033	0.69		0.67	
4725.81	[Ne IV] 4725.62	0.61	17%	0.033	0.64	1.20	0.48	
4740.25	[Ar IV]+? 4740.20	5.60		0.029	5.86	6.17	5.89	
4816.30	4816.3			0.011			0.11	
4859.38	Si II 4860.3	2.77	23%	0.000	2.77	2.77		
4861.35	H I (β) 4861.33	100.00	3%	0.000	100.00	100.00	100.00	100.00
4893.40	[Fe VII] 4893.4			-0.008		0.04		
4921.90	He I 4921.93	1.06	17%	-0.014	1.04	0.48	0.66	
4931.43	[O III] 4931.30	0.17		-0.017	0.16	0.37	0.33	
4948.77	4948.6?	0.17	15%	-0.021	0.16			
4958.95	[O III] 4958.92	384.01	1%	-0.023	370.04	398.11		
4969.49	[Fe VI] 4969.00	0.18		-0.026	0.17			
4972.92	[Fe VI] 4872.1	0.14		-0.026	0.13	0.05		
4985.56	[Fe VII] 4988.6	0.08		-0.029	0.08			
4988.96	[Fe VII] 4984.6?	0.05	14%	-0.030	0.05			
4996.32	4996.4?	0.46	3%	-0.032	0.44			
5006.79	[O III] 5006.84	1222.64		-0.034	1158.31	1174.90		1202.00
5015.89	He I 5015.68	1.26		-0.036	1.19	0.37		
5017.71		0.57		-0.036	0.54			
5028.42	5028.2	0.12		-0.039	0.11			
5029.73	5029.6	0.09		-0.039	0.09			
5047.70	He I 5047.74			-0.043		0.05		
5056.48	Si II 5056.35	0.10		-0.045	0.09			
5058.95	line?	0.08		-0.045	0.07			
5060.25	line?	0.04		-0.046	0.04			
5131.15	5131.2	0.14	6%	-0.060	0.13			
5145.97	O I? 5146.06	0.15	20%	-0.063	0.13	0.11		
5151.90	[Fe III] 5151.9			-0.065		0.03		
5159.02	[Fe II] 5158.81	0.09		-0.066	0.08	0.07		
5176.55	[Fe VI] 5176.4	0.12	11%	-0.070	0.11	0.07		
5181.68	line?	0.12		-0.071	0.11			
5191.76	[Ar III] 5191.80	0.12	13%	-0.073	0.11	0.10		
5198.10	[N I] 5197.90	0.18		-0.074	0.16			
5200.43	[N I] 5200.26	0.12		-0.075	0.11	0.15		
5202.26	line?	0.06		-0.075	0.06			
5228.93	5229?	0.17		-0.080	0.15			
5249.76	5250?	0.13		-0.084	0.12			
5261.56	[Fe II] 5261.61	0.05		-0.087	0.05			
5270.80	[Fe III] 5270.40	0.06	27%	-0.089	0.05	0.04		
5277.80	[Fe VI] 5277.8	0.08	65%	-0.090	0.07	0.03		

125

TABLE 2B—*Continued*

λ(Å)	Identification	F(Ham)	RMS	f(λ)	I(Ham)	I(ITS)	I(ptg)	I(P.E.)
5309.27	[Ca V] 5309	0.14	9%	-0.097	0.12	0.09		
5323.08	[Cl IV] 5323.3	0.08	2%	-0.100	0.07	0.05		
5335.43	[Fe VI] 5335.3	0.11	14%	-0.102	0.10	0.05		
5346.07	5346?	0.12	11%	-0.105	0.10			
5361.31	5363?	0.11		-0.108	0.09			
5411.55	He II/[Fe III] 5412	5.77	11%	-0.118	4.79	3.98		
5424.34	[Fe VI] 5423.9	0.07	9%	-0.121	0.06	0.04		
5426.61	[Fe VI] 5426.6	0.04	16%	-0.121	0.03			
5460.34	line?	0.48		-0.128	0.39			
5470.83	5470.9	0.04	40%	-0.130	0.03			
5485.04	[Fe VI] 5484.9	0.07	22%	-0.133	0.06	0.05		
5517.69	[Cl III] 5517.71	0.41	12%	-0.139	0.33	0.26		
5537.80	[Cl III] 5537.88	0.46	11%	-0.143	0.37	0.30		
5576.65	[OI] 5577	1.54		-0.152	1.21			
5592.31	O III 5592.37	0.11	3%	-0.155	0.08	0.05		
5631.08	[Fe VI] 5630.9	0.08	10%	-0.164	0.06			
5649.87	5650	0.02		-0.168	0.02			
5660.05	5660	0.04		-0.170	0.03			
5676.92	[Fe VI] 5677	0.08	4%	-0.174	0.06			
5697.09	C III 5696?	0.06	58%	-0.178	0.04			
5721.23	[Fe VII] 5721.1	0.13	4%	-0.184	0.10	0.48		0.51
5754.48	[N II] 5754.64	0.63	11%	-0.191	0.47	0.12		
5801.36	C IV 5801.51	0.43	7%	-0.201	0.31	0.02		
5806.76	He II 5806.3	0.05	29%	-0.202	0.04	0.09		
5812.01	C IV 5812.14	0.23	7%	-0.203	0.17			
5820.40	He II/[NiIV]5820	0.05	12%	-0.205	0.03			
5828.48	He II 5828.6	0.08	21%	-0.206	0.05			
5837.08	He II 5836.3	0.07	8%	-0.208	0.05			
5846.80	He II 5847.1	0.07	11%	-0.210	0.05			
5857.18	He II 5858?	0.06	3%	-0.212	0.04	0.02		
5858.30	He II 5858.3			-0.212				
5867.72	He II 5867.8+?	0.18	12%	-0.214	0.13	0.03		
5869.00	He II 5868?	0.06	20%	-0.215	0.04			
5875.59	He I 5875.67	10.72	5%	-0.216	7.64	7.24		11.74
5882.12	He II 5882.4	0.08	4%	-0.217	0.06	0.05		
5896.59	He II 5896.9	0.07		-0.220	0.05	0.04		
5913.07	He II 5913.5	0.09	14%	-0.223	0.06	0.06		
5914.93	He II?	0.09		-0.223	0.07			
5931.97	He II?	0.11	10%	-0.226	0.08	0.06		
5945.52	5944?	0.03		-0.228	0.02			

λ(Å)	Identification	F(Ham)	RMS	f(λ)	I(Ham)	I(ITS)	I(ptg)	I(P.E.)
5952.92	He II 5953.1	0.12	7%	-0.229	0.08	0.07		
5977.12	He II 5977	0.13	3%	-0.234	0.09	0.07		
6004.76	He II 6004.8	0.12	8%	-0.238	0.09	0.07		
6010.63	6010?	0.03		-0.239	0.02			
6036.99	He II 6037.2	0.18	7%	-0.243	0.12	0.08		
6048.23	atm?	0.20		-0.245	0.13			
6051.78	line?	0.37		-0.246	0.25			
6074.26	HeII 6074.3	0.18	10%	-0.249	0.12	0.10		
6086.92	[Ca V]/[FeVII]	0.21	9%	-0.252	0.14	0.07		
6101.68	[K IV] 6101.80	0.47	4%	-0.254	0.32	0.21		
6113.26	line?	0.16		-0.256	0.11			
6116.12	line?	0.96		-0.256	0.64			
6118.28	He II 6118.3	0.19	4%	-0.257	0.13	0.08		
6133.00	[Fe III] 6133.0			-0.259		0.08		
6151.40	6151.4			-0.262		0.04		
6165.74	[Mn V] 6166.2	0.06		-0.264	0.04			
6170.77	He II 6170.7	0.24	9%	-0.265	0.16	0.09		
6221.13	[Mn V] 6221.86	0.02		-0.273	0.01			
6233.89	He II 6233.8	0.28	5%	-0.275	0.18	0.14		
6293.77	line?	0.10		-0.284	0.07			
6300.17	[O I][a] 6300.30	1.88	6%	-0.285	1.20	1.15		3.55
6306.46	line?	0.09		-0.286	0.06			
6311.99	[S III] +? 6312.10	2.06	14%	-0.287	1.32	1.02		1.86
6363.64	[O I] 6363.78	0.70	10%	-0.294	0.44	0.36		
6371.35	Si II 6371.36	0.03		-0.295	0.02			
6406.30	He II 6406.5	0.45	9%	-0.301	0.28	0.50		
6434.71	[Ar V] 6435	2.14	17%	-0.305	1.32	0.55		
6526.92	6527?	0.60	6%	-0.318	0.37			
6544.37	line?	0.15	15%	-0.320	0.09			
6547.87	[N II] 6548.03	8.86	12%	-0.321	5.36	6.03		
6560.06		15.62	8%	-0.322	9.44			
6562.64	H I (α) 6562.82	468.80	8%	-0.323	282.84	281.84		276.00
6577.67	C II 6578.03	0.20		-0.325	0.12			
6580.88	line?	0.10		-0.325	0.06			
6583.08	[N II] 6583.41	28.50	9%	-0.326	17.12	19.95		49.00
6677.92	He I 6678.15	2.91	2%	-0.338	1.71	1.86		3.39
6683.06	He II 6684	0.74	0%	-0.339	0.43			
6716.20	[S II] 6716.47	1.46		-0.343	0.86	0.91		
6730.52	[S II] 6730.85	2.30	5%	-0.345	1.34	1.55		6.76
6850.02	6850	0.04		-0.359	0.02			

126

TABLE 2B—Continued

λ(Å)	Identification	F(Ham)	RMS	f(λ)	I(Ham)	I(TS)	I(ptg)	I(P.E.)
6890.72	He II 6891	0.97	0%	-0.363	0.55	0.32		
7005.55	[Ar IV] 7005	3.74	5%	-0.376	2.08	1.41		
7062.09	line?	0.09		-0.383	0.05			
7065.01	He I 7065.28	5.60	4%	-0.383	3.07	3.31		4.90
7135.64	[Ar III] 7135.78	13.11	6%	-0.391	7.12	6.76		9.55
7170.52	[Ar IV] 7170.62	0.58	2%	-0.394	0.31			
7177.40	He II 7178	1.16	2%	-0.395	0.63	0.65		
7237.50	[Ar IV] 7237.54	0.48		-0.401	0.26	0.20		
7263.02	[Ar IV] 7262.70	0.44	6%	-0.404	0.23	0.19		
7281.15	He I 7281.35	0.69	6%	-0.406	0.37	0.36		
7319.61	[O II] 7319.65	2.16	0%	-0.410	1.14			
7329.88	[O II] 7330.16	1.82	0%	-0.411	0.96	2.82		6.92
7530.26	[Cl IV] 7529.90	0.66	10%	-0.430	0.34	0.32		
7592.36	HeII 7593	1.05	12%	-0.436	0.53	0.26		
7703.00	7702?	0.05		-0.447	0.03			
7712.66	7713?	0.09		-0.448	0.05			
7725.94	[S I] 7726	0.38	8%	-0.449	0.19	0.10		
7750.97	[Ar III] 7751.12	3.05		-0.451	1.50	1.95		
8045.49	[Cl IV] 8046	1.54	15%	-0.477	0.73	0.78		
8179.59	line?	0.16		-0.488	0.07			
8187.07	line?	0.13		-0.488	0.06			
8196.63	8197?	0.28		-0.489	0.13	0.27		
8204.15	line?	0.12		-0.490	0.05			
8236.67	He I/H I 8237	2.51		-0.492	1.16	0.85		
8276.78	H Iª (P 32) 8276.3	0.14		-0.496	0.07			
8280.76	H Iª (P 31) 8281.1	0.19		-0.496	0.09			
8286.87	H I (P 30) 8286.43	0.17		-0.496	0.08			
8291.84	H I (P 29) 8292.31	0.17		-0.497	0.08			
8298.30	H I (P 28) 8298.84	0.22		-0.497	0.10			
8305.38	line?	0.09		-0.498	0.04			
8306.97	H I (P 27) 8307	0.10		-0.498	0.05			
8314.72	H I (P 26) 8314.26	0.22		-0.499	0.10			
8323.10	H I (P 25) 8323.43	0.17	0%	-0.499	0.08			
8333.67	H I (P 24) 8333.78	0.18	5%	-0.500	0.08			
8345.10	H I (P 23) 8345.55	0.15	14%	-0.502	0.07			
8349.60	line?	0.35		-0.503	0.16			
8358.81	H I (P 22) 8359.01	0.26		-0.504	0.12			
8374.26	H I (P 21) 8374.48	0.26	2%	-0.506	0.12			
8377.65	line?	0.17		-0.507	0.08			
8392.22	H I (P 20) 8392.40	0.37		-0.509	0.17			
8413.20	H I (P 19) 8413.32	0.45		-0.512	0.20			
8419.72	8426?	0.19		-0.513	0.09			
8437.82	H I (P 18) 8437.96	0.39		-0.516	0.18			
8466.99	H I (P 17) 8467.26	0.47	10%	-0.521	0.21			
8469.93	line?	0.15		-0.521	0.07			
8480.28	He I 8480.73	0.07		-0.523	0.03			
8499.12	line?	0.09		-0.525	0.04			
8502.07	H I (P 16) 8502.49	0.68	0%	-0.526	0.30			
8502.84	[Cl III] 8503	0.84		-0.526	0.37			
8519.38	HeII 8519	0.06		-0.528	0.02			
8545.06	H I (P 15) 8545.38	0.73	16%	-0.532	0.32			
8575.84	[Cl II] 8578.7?	0.10		-0.537	0.04			
8579.26	[Cl II] 8578.70	0.05		-0.537	0.02			
8594.92	line?	0.13		-0.540	0.06			
8598.33	H I (P 14) 8598.39	0.87	11%	-0.540	0.38			
8648.58	He I 8648.26	0.05		-0.548	0.02			
8664.83	H I (P 13) 8665.02	1.41	14%	-0.550	0.60			
8701.33	line?	0.08		-0.555	0.03			
8707.68	line?	0.15		-0.556	0.06			
8746.51	line?	0.09		-0.562	0.04			
8750.23	H I (P 12) 8750.48	1.76		-0.562	0.73			
8798.84	line?	0.12		-0.569	0.05			
8862.56	H I (P 11) 8862.79	1.93		-0.578	0.78			
8873.59	line?	0.18		-0.579	0.07			
9014.27	H I (P 10) 9014.91	2.76		-0.599	1.08			
9068.99	[S III] 9068.90	15.39	2%	-0.606	5.96			
9228.75	H I (P 9) 9229.02	4.42	30%	-0.612	1.69			
9530.74	[S III]ª 9531.	53.71	12%	-0.620	20.35			
9545.84	H Iª(P 8)9545.9	5.24	12%	-0.620	1.98			
9762.80	He I 9762	0.19		-0.625	0.07			
10045.12		0.49		-0.631	0.18			
10049.11	H I (P 7) 10049.38	9.36	5%	-0.631	3.48			
10123.23	HeII 10123.6	30.24		-0.633	11.23			

Col. (6).—I*(IUE) (Table 2A): from Marionni & Harrington 1981.
Col. (9).—IUE data (Table 2A): our remeasurements (NSSDC Archive Data); asterisks and parenthesis (Table 2B): from photoelectric data of Kaler, Czyzak, & Aller 1968.
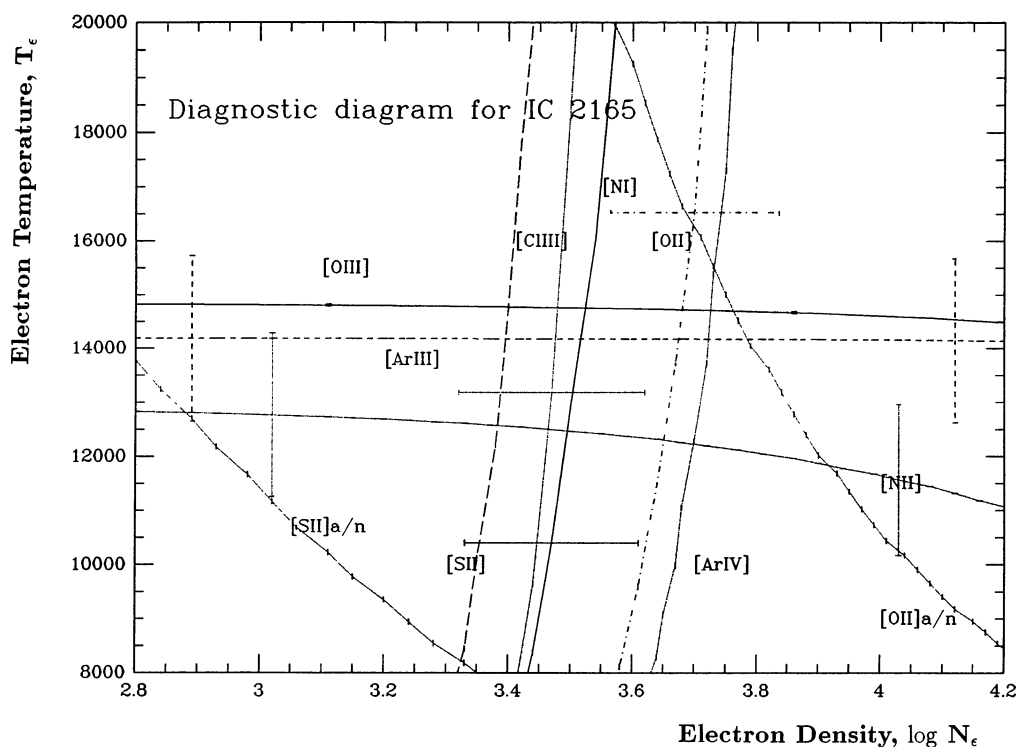ª Affected by atmosphere.

I*(IUE) in Column (6): from Marionni, P.A. and Harrington, J.P. (1981).

IUE data in Column (9): Our remeasurements (NSSDC Archive Data).

(*) in Column (9): from Photoelectric Data from Kaler et al.(1968).

(") in Column (2): affected by atmosphere.

127

FIG. 1.—Diagnostic diagram for IC 2165. The error bars are added in the vertical direction for ions such as O III that fix T_ϵ, and horizontally for ions such as O II that fix N_ϵ.

on both electron density and temperature. These ratios are listed in Table 3 for each available ion. I have determined the diagnostic electron temperature and density curves from all practicable observed forbidden line intensity ratios. These diagnostic curves, (N_ϵ, T_ϵ), were obtained with the aid of recently available electronic collision strengths, for instance, from Butler & Zeippen (1989) for [Cl III], and from Zeippen, Butler, & Le Bourlot (1987) for [Ar IV]; otherwise we have relied on the compilation by Mendoza (1983) for most other ions. The diagnostics are often not mutually consistent—an effect that can be due to (1) actual variations in density and temperature because, e.g., [S II] and [Ar IV] probably arise in different strata; (2) inaccuracies in atomic parameters; or (3) observational errors.

Figure 1 shows electron density and temperature relations corresponding to the Hamilton echelle observations of [N I], [N II], [O II], [O III], [S II], [S III], [Cl III], [Ar III], and [Ar IV]. For most ions in Figure 1 the error bars were added in the vertical direction for the temperature-sensitive diagnostic lines, but were omitted for some ratios, such as [Ar IV] and [O II] auroral/nebular line ratios which depend strongly on both T_ϵ and N_ϵ. The electron temperature is determined as $T_\epsilon \simeq$ 15,000 K from the [O III] ratio, but possibly a little lower, $\sim$13,000 ± 1400 K, suggested by [Ar III], or $\sim$12,500 ± 1500 K, suggested by [N II], on the diagram. Most of the primarily density-dependent line ratios, plotted in Figure 1, pass through the [O III] and [Ar III] curves for 2300 cm^{-3} < N_ϵ < 5500 cm^{-3}. The auroral/nebular line ratio, [O II] λ3727/(λ7319 + λ7330), suggests an even higher density (9000 cm^{-3}). However, the other auroral/nebular line ratios, [S II] (λ6716 +

λ6731)/(λ4069 + λ4079) and [S III] (λ9069 + λ9531)/λ6312 show poor results, because the weak [S II] λ6716 is strongly contaminated by "bleeding" from Hα drip, and the measurements of [S III] λ6312 also might not be suitably corrected for blending with the He II λ6310 line. [S III] λ9531 is also severely impacted by water vapor. These two line ratios show a big discrepancy with the others; thus we have to rely on the former line ratios. In summary, the diagnostics indicate that the bulk

TABLE 3
DIAGNOSTIC LINE RATIOS: IC 2165

Ion	Lines	Ratio	Quantities Determined
[N I]	$I(\lambda 5200)/I(\lambda 5198)$	0.67	N_ϵ
[N II]	$I(\lambda 6548 + \lambda 6583)/I(\lambda 5755)$	54.68	N_ϵ, T_ϵ
[O II]	$I(\lambda 3729)/I(\lambda 3726)$	0.51	N_ϵ
[O II][a]	$I(\lambda 3727)/I(\lambda 7319 + \lambda 7330)$	4.56	N_ϵ, T_ϵ
[O III]	$I(\lambda 4959 + \lambda 5007)/I(\lambda 4363)$	94.01	T_ϵ
[S II]	$I(\lambda 6716)/I(\lambda 6731)$	0.66	$N_\epsilon, (T_\epsilon)$
[S II][a]	$I(\lambda 6716 + \lambda 6731)/I(\lambda 4069 + \lambda 4076)$	94.01	N_ϵ, T_ϵ
[S III]	$I(\lambda 9069 + \lambda 9531)/I(\lambda 6312^b)$	33.76	N_ϵ, T_ϵ
[Cl III]	$I(\lambda 5518)/I(\lambda 5538)$	0.89	$N_\epsilon, (T_\epsilon)$
[Ar III]	$I(\lambda 7136 + \lambda 7751)/I(\lambda 5191)$	113.58	T_ϵ
[Ar IV]	$I(\lambda 4711)/I(\lambda 4740)$	1.11	N_ϵ

NOTE.—These ratios are only from the Hamilton echelle CCD 800 × 800 chip data.
[a] Auroral/nebular ratios.
[b] Contaminated by He II.

of the optical radiation arises from strata with relatively high electron temperatures ($T_e = 13{,}000$–$15{,}000$ K) whose densities are of the order of 2300–5500 cm^{-3}.

We chose various temperatures and densities on the basis of the diagnostic diagrams to obtain the ionic concentrations. Table 4 lists the results for each species. Successive columns in the table give the ion and the wavelengths of the lines involved, their intensities corrected for interstellar reddening, the electron temperatures and densities selected for the actual calculation of the ionic concentration, $N(i)/N(H^+)$ as computed from appropriate equations of statistical equilibrium, and the adopted sums of all the observed ionic concentrations for each element in terms of $N(H^+)$. For optical region lines the ionic concentrations are calculated from the Hamilton echelle data, and for the ultraviolet lines we use results from measurements

listed in column (9) of Table 2. Estimation of the ionic concentration of He I is complicated by the metastability of the lowest triplet level, $2s\,^3S$, which can have a significant population at high temperatures and densities. Clegg (1987) has given a formula for C/R, the ratio of level excitations by collisions to those by recombination, whereby the upper limit to the collisional contribution for any He I line is calculated. We applied these correction factors to the normally used He I lines, $\lambda\lambda 4471$, 5876, 6678, and 7065 and ignored the results from He I $\lambda\lambda 3889$, 5876, 6678, and 7065 (because of optical depth effects, and because He is blended with H in $\lambda 3889$!). Disagreement in He II might be due to the errors in the flux calibrations.

Except for He, only a fraction of the total number of atoms of a given element contribute to normally observed lines. For most elements the sum of the observed ionic concentrations

TABLE 4
IONIC CONCENTRATIONS: IC 2165

Lines (1)	I_{corr} (2)	T_e (3)	N_e (4)	$N(i)/N(H^+)$ (5)	$\Sigma[N(i)/N(H^+)]$ (6)
He I $\lambda 6678$	1.71	12500	4000	0.1258	$(\times)^a$
He I $\lambda 4471$	2.81	12500	4000	0.0584	
He I $\lambda 5876$	7.64	12500	4000	0.0504	
He I $\lambda 7065$	3.07	12500	4000	0.1794	$(\times)$
He II $\lambda 4686$	59.49	14500	4000	0.0529	
He II $\lambda 5412$	4.84	14500	4000	0.0316	0.1073
C II $\lambda\lambda 2325, 2329$	77.98	12500	4000	4.24E−05	
C III $\lambda\lambda 1907, 1909$	943.17	14000	4000	2.53E−04	
C IV $\lambda\lambda 1549, 1551$	1030.91	15000	4000	1.12E−04	4.08E−04
N I $\lambda\lambda 5198, 5200$	0.27	11500	4000	2.49E−07	
N II $\lambda\lambda 6548/6584, 5755$	22.94	12500	4000	1.98E−06	
N III $\lambda\lambda 1747–1754$	32.82	14500	4000	2.63E−05	
N IV $\lambda\lambda 1483–1487$	32.53	15500	4000	1.84E−05	
N V $\lambda\lambda 1239, 1243$	71.79	16500	4000	1.64E−05	6.33E−05
O I $\lambda\lambda 6300, 6363$	2.88	11500	4000	2.00E−06	
O II $\lambda\lambda 3727, 7319/7330$	29.88	12500	4000	7.85E−06	
O III $\lambda\lambda 4959, 5007$	1528.02	14500	4000	1.43E−04	
O III $\lambda 4363$	20.74	14500	4000	1.52E−04	
O III $\lambda\lambda 1658, 1666$	30.46	14500	4000	8.75E−05	1.37E−04
F III $\lambda\lambda 5723, 5724$	0.10	14500	4000	1.11E−06	1.11E−06
Ne III $\lambda\lambda 3868, 3967$	111.52	14500	4000	1.94E−05	
Ne IV $\lambda\lambda 2423, 2425$	121.95	14500	4000	3.23E−05	
Ne IV $\lambda\lambda 4724–4726$	2.23	14500	4000	4.79E−05	
Ne IV $\lambda 1602$	11.64	14500	4000	2.13E−04	5.95E−05
Mg V $\lambda\lambda 2784, 2927$	7.70	17000	4000	2.30E−06	2.30E−06
Si III $\lambda\lambda 1884, 1892$	9.29	14500	4000	4.08E−07	4.08E−07
S II $\lambda\lambda 6717, 6731$	2.20	12500	4000	4.89E−08	
S II $\lambda\lambda 4068, 4076$	1.57	12500	4000	1.30E−07	
S III $\lambda 6312$	1.32	13500	4000	9.70E−07	
S III $\lambda\lambda 9069, 9552$	26.31	13500	4000	5.53E−07	
S IV $\lambda 10.5\,\mu m$	34.50	14500	4000	9.40E−07	2.00E−06
Cl III $\lambda\lambda 5517, 5537$	0.70	14000	4000	2.01E−08	
Cl III $\lambda\lambda 8481, 8501$	0.41	14000	4000	3.37E−07	
Cl IV $\lambda\lambda 7530, 8045$	1.10	15000	4000	3.22E−08	
Cl IV $\lambda 5323$	0.07	15000	4000	3.81E−08	5.52E−08
Ar III $\lambda\lambda 7535, 7751$	8.82	14000	4000	2.96E−07	
Ar III $\lambda\lambda 5192$	0.11	14000	4000	3.04E−07	
Ar IV $\lambda\lambda 4711, 4740$	11.19	15000	4000	3.68E−07	
Ar IV $\lambda\lambda 7265/7240, 7173$	0.82	15000	4000	1.57E−06	
Ar V $\lambda\lambda 6435, 7005$	3.48	15500	4000	1.57E−07	8.25E−07
K IV $\lambda 6103$	0.32	14500	4000	3.64E−08	
K V $\lambda\lambda 4122, 4163$	0.14	15500	4000	1.97E−08	5.61E−08
Ca V $\lambda 5309$	0.12	14500	4000	3.11E−08	3.11E−08

^{a} ($\times$): ignored because of optical depth effects (see text).

does not give us $N(\text{element})/N(H^+)$. Two methods for establishing the ionization correction factor are frequently used in determining abundances. One method is to use a simple extrapolation scheme, with representative temperature(s) and density(ies) determined from the observations themselves. This approach has been used by many investigators—for example, by Barker (1983) for NGC 7009 and by TPP for IC 2165. It treats all the emission as if it came from one or a few temperature and density zones, and requires a simple proportionality or an empirical correction for unobserved stages of ionization. The other method is by calculating a photoionization model which may supply an interpolation device. This method is used, for instance, by Keyes, Aller, & Feibelman (1990) for NGC 7027. Although it is conceptually reasonable for any given object, it may smooth over most of the actual density fine structure. This is the method I have adopted, but it cannot be properly implemented until we find a nebular model that gives good line predictions.

4. IONIZATION AND THERMAL EQUILIBRIUM OF A PLANETARY NEBULA

Because nebular emission results from the photoionization of a diffuse gas by ultraviolet photons from a hot PNN, the ionization and thermal equilibrium should be fixed for a constituent ion at each radial point. General descriptions for physical processes in gaseous nebulae and relevant equations are given by, e.g., Aller (1984) and Osterbrock (1989). Our nebular program is now based on the radiative transfer solution rather than on the so-called on-the-spot approximation which has been used in much previous work. We assumed a steady state and a uniform density in a nebular shell, at least in initial endeavors. Several conditions for a steady state must be fulfilled.

4.1. *Ionization Equilibrium*

For any particular ion, the number of photoionizations per unit time must equal the corresponding recombination rate. In practice, we should also consider the role of charge exchange for elements other than H and He. The electron density at any point will depend on the degree of ionization of H, He, and He^+. The role of other ions can be neglected.

4.2. *Thermal Equilibrium*

For any particular volume element in the PN the electron kinetic temperature is determined by requiring that the gas be in thermal equilibrium. The energy gained by the electrons through photoionization, therefore, must be balanced against the corresponding emission losses due to recombination, which is followed by radiative decay, collisional excitation, and thermal bremsstrahlung.

The question of energy balance was first discussed in a quantitatively realistic manner in a series of papers entitled "Physical Processes in Gaseous Nebulae" by Menzel and coworkers; see especially Menzel, Aller, & Baker (1938), where the basic equations are set up, and Baker, Mendez, & Aller (1938), where they are solved. See also Menzel & Aller (1941) and Spitzer (1948), who formulated the problem for energy balance in the continuum.

Among objects of lower excitation, cooling is mainly by collisional excitation of low-lying levels of abundant ions of C^+, C^{++}, N^+, O^+, O^{++}, etc. In a low-density nebula excited by a very high temperature PNN, H^0 and H^+ can coexist over an extensive region in which hydrogenic radiative cooling can be important if $T_e = 20{,}000$ K. Appropriate expressions for atomic hydrogen cooling by electron collisional excitation may be obtained from Hummer & Seaton (1963) and Harrington (1967).

In a nebula of moderate density a number of atoms may accumulate in the high $2\,^3S$ metastable level ($\chi \sim 20$ eV) of He I. Collisions of electrons with He atoms in this term can excite them to higher levels or even ionize them, resulting in a drain of energy. Following the Clegg (1987) and Clegg & Harrington (1989) studies on He I collisional effects and cooling, we can also evaluate the energy losses per unit volume per second by He I ($2\,^3S$). These refinements are needed to predict properly the intensities of He I emission lines, e.g., $\lambda\lambda4471$, 5876, 6678, 7065, and 10830. The He I $2\,^1S$ level is also highly metastable. Collisions with electrons here can excite He atoms to higher singlet and triplet terms and produce ionization.

The $2\,^2S$ level of H is also metastable, and a substantial population can be built up in this level, so a similar effect could occur also when the Lyman-α flux is large. Atoms can be pumped into $2\,^2P$ and be shifted by collisions to $2\,^2S$. The collisional cooling contribution from these metastable states is not significant enough to be considered. However, the aforementioned H collisional cooling by excitation from the ground level should be properly treated, since its contribution is comparable to that of a heavy ion, e.g., C^{++}.

4.3. *The Diffuse Radiation*

The diffuse radiation sources are recombinations to the ground states of H^0, He^0, and He^+, recombinations to the $n = 2$ level of He^+, single-photon decay from $He^0\ 2\,^3S$, two-photon decays from He^+ and He^0, and the He^+ Lyman-α line and the radiation produced by the degradation of He^+ Lyman-α by the Bowen fluorescence mechanism. For the evaluation of the integrals in the ionization equilibrium equations with the above various radiation components, we choose 61 intervals (increased from the previously used number of 35). These are carefully selected to divide the range from 10.5 to 234 eV into appropriate segments. The integration over all 61 intervals is evaluated by the trapezoidal rule. The relevant basic equations and discussions are found in Harrington (1991), Harrington et al. (1982), and Harrington (1967) and also in Hyung (1992).

5. DEVELOPMENT OF A THEORETICAL COMPOSITE-SHELL MODEL

5.1. *Introduction*

Theoretical models have been recognized as helpful for interpreting the spectra of planetary nebulae. Among practical nebular modeling programs, one developed long ago by B. Balick and revised and updated mostly by C. D. Keyes was used for a PN survey (Aller & Keyes 1987), for NGC 7027 (Keyes et al. 1990), and for objects in the Magellanic Clouds (Aller et al. 1987).

The Balick-Keyes program, originally formulated for low- to moderate-excitation PNs, made some crude approximations in solving the thermal balance equation and did not handle effects that can be important in high-excitation PNs. For example, it included the stellar UV radiation field only up to 135 eV (~ 10 rydbergs), employed the OTS approximation, and did not consider the influence of radiative transfer. It did not consider collisional cooling by H and He or the role of their high metastable levels. It did not take into account two-photon UV emissions and UV emission from He, which can be important at high T_e.

The present program adopts innovations such as collisional cooling by H and He and the Lyman-α escape probability, and recognizes the role of radiative transfer, as introduced by Harrington (1967). It also extends the effective range of the UV radiation field (which involves the attenuated stellar radiation and the diffuse component) from 10 up to 210 eV. The program is also able to accommodate all significant chemical elements and recognizes that the principal heavier elements such as C, N, O, and Ne can influence the radiation field even though their abundances are $\sim 10^{-3}$ to $\sim 10^{-4}$ times that of H. If a program does not include contributions from these heavier existing elements, the resulting ionization model and its predictions may be affected by a small but not always totally negligible amount. A typical nebular model calculation with either the Balick-Keyes or the Harrington program requires about 5 minutes to run with a VAX-4000/MODEL-300, while the new program requires more than an hour because of additional features employed. In the first approximation we assume nebulae to be of uniform chemical composition. This appears to be true for most PNs (J. B. Kaler 1990, private communication), but some striking exceptions are known, notably Abell 30 and Abell 78 (Jacoby & Ford 1988). Input parameters in the nebular program are the following: the stellar radius, the stellar flux distribution, the nebular geometry including any variation $N_{\rm H}(r)$, the nebular hydrogen density, and elemental abundances. Once these are given, the program integrates radially outward. One typically starts with a step of about 0.0001 times the nebular size, computing gas opacities, ionization states of the constituents, and electron temperatures. Heating is provided by the energy input from the radiation field, which comprises geometrically diluted starlight and diffuse radiation. The flux is also modified by absorption by the nebular gases between the star and the point in question. The cooling processes are as described above. An iterative energy balance solution is sought for each mesh point; the routine then predicts the line and continuum intensities.

Finally, one must compare prediction with observed line intensities. Furthermore, the mean theoretical electron temperature T_e found by the energy balance condition should be in accord with the plasma diagnostic T_e found from appropriate forbidden lines as described in § 3.4.

5.2. Calculation of the Flux from a Slot of Arbitrary Size and Position in a Composite-Shell Model

Although the nebular density distribution as a function of distance r from the central star (PNN) may depend on polar coordinates θ, ψ, a simple radial density variation or a constant density throughout the PN is usually introduced initially. The

density in different regions of a PN can be obtained, for example, from line ratios such as [S II] $\lambda 6716/\lambda 6731$, which also gives us the electron temperature information at the observed position if we get also the transaural lines $\lambda\lambda 4068$ and 4076. However, the density that is indicated by a particular line ratio does not necessarily represent the overall density distribution within a PN. It is hoped that the density distribution can be chosen in such a way that the emissivity of the gas would reproduce the observed isophotes. Given the distance of the nebula, we can thus fix the distribution of the gas about the star, and therefore the dilution of the radiation at each point.

Many authors have suggested a "composite-shell" structure that has a density contrast between the equatorial ring and polar conical shells to explain ellipsoidal or "flat-ring" structures. This geometry, however, has not been applied directly to an ionization modeling of spectroscopic data, because of complications arising from radiative transfer effects. Apparently many objects that exhibit a nonspherical symmetry, such as an elliptical ring, can be explained by introducing the simple geometry of a ring-cone shell with an appropriate projection angle in the sky plane. The essential parameters are the densities in the equatorial ring and polar conical shells, their sizes, and the tilt of the axis of symmetry upon the sky plane.

Figure 2 depicts the composite-shell/cone structure. The radial distribution of densities in each section should be adjusted
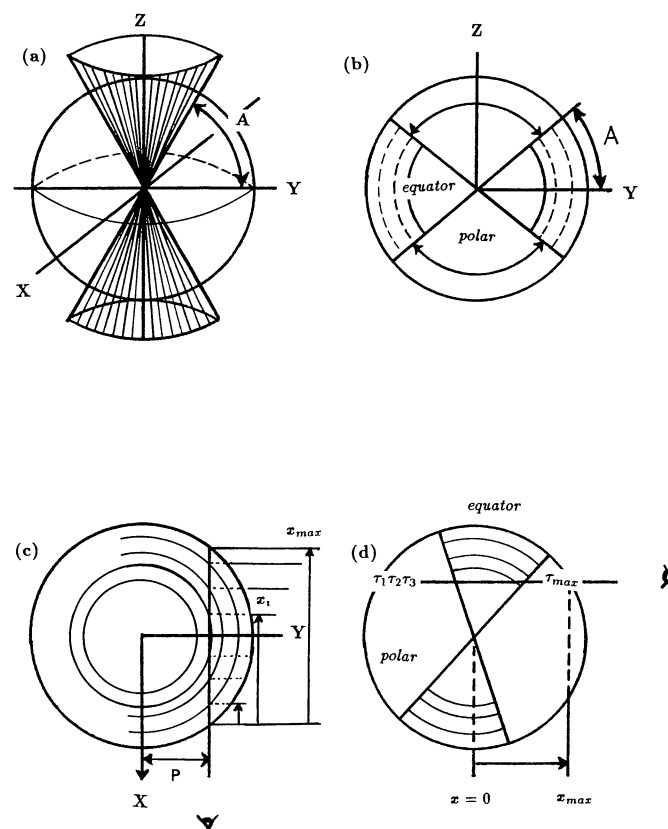

Fig. 2.—(a) Diagram of the model used; (b–d) cross sections. (b) Edge-on view ($i = 90°$) showing density contrast and opening angle A; (c) face-on view (i.e., from pole) showing path length x_i and impact parameter p; (d) situation in which the nebular axis of symmetry is tilted slightly ($i \sim 0°$) with respect to the sky plane.

so that the emissivity of the gas reproduces the appearance of the PN. A polar cone of one density structure, $N_p(r)$, and a toroid or ring of another, $N_e(r)$, are adopted in the structure of Figure 2a. Figure 2b gives a cross section of the nebula through the axis of symmetry. The angle A depicts the spread of the equatorial zone. For $A = 90°$ we have a simple spherical structure. For an assumed equatorial angle A we can determine whether a volume segment $P(x, y, z)$ along the impact parameter p belongs to the polar cone or to the equatorial ring with the following simple relation:

$$A \leq \tan^{-1} \frac{z}{(y^2 + x_i^2)^{1/2}} \quad \text{(polar)},$$

$$A > \tan^{-1} \frac{z}{(y^2 + x_i^2)^{1/2}} \quad \text{(equator)},$$

where an impact parameter $p = (y^2 + z^2)^{1/2}$ and a path length $x_i^2 = r_i^2 - p^2$, since an observer looks along line x.

The foregoing relation is very simple in the Figure 2 model geometry. However, if a model nebula is viewed from an arbitrary angle away from the equatorial plane, the line of sight passes through both the less dense (i.e., polar) and more dense (i.e., equatorial) shells. To handle this projection effect of the nebula, a coordinate transformation of the Euler rotation is introduced in the nebular modeling. When the polar axis of a PN is aligned in the line of sight (x), the equatorial shell will appear as a perfectly circular ring shape in the sky plane (y, z). A cross section for a face-on view is given in Figure 2c, where a small path length, denoted x_i, is shown for a impact parameter p. In general, the inclination will not be $i = 0°$ or $i = 90°$; we need to consider a PN oriented at an arbitrary inclination angle as shown in Figure 2d.

In the modeling procedure, the line spectra and continuum calculation are done in the grid space of a PN; first, one large volume which includes the nebular geometry will be subdivided into many tiny fractional volume elements, for example, $150 \times 150 \times n_i$, where n_i can be determined by the number of the radial shells (x_i) along the line of sight at the impact parameter p. Then the brightness map (for line emission) at 150×150 points of sky surface will be obtained after adding up all n_i of the surface brightness contributions along the line of sight in the grid space.

The density parameters and both the projection and the equatorial angles in the proposed model calculations are the three main parameters that are intended to explain the nebular appearance. For the given angle A of the equatorial shell and the Euler rotation angles in model calculations, the resulting map can be drawn from grid calculations of surface brightness for any chosen particular line, for example, [O III] $\lambda5007$ and [N II] $\lambda6584$, and can be compared with the observed isophote maps.

The geometrical parameters, viz., the projection angles to the sky and the densities of shells, must be modified until the model reproduces in a satisfactory way the appearance of the target PN. What is more, the model prediction also should fit the spectra coming from the small area of the nebula within the slot in our series of observations and also from different areas selected by other observers. A successful three-dimensional geometrical model, which correctly handles the physical processes in the gas including effects of dust if need be, must reproduce the line spectra and the isophotes.

This method of summing up the emission along the line of sight in the grid space permits one to include simultaneously the proper slot size of observations and the geometrical structures of the project nebulae. Thus, in treating the spectral data, one must carefully check the slot size used in the observations and its placement on the image; the fraction of the target nebular size varies for each object. For relatively small objects—for example, IC 2165—a substantial fraction of the main part of the PN including the central star PNN could be covered within the slot so that the spectra might represent a fair percentage of the whole nebula. The observed fractional area of IC 2165 included in the Hamilton echelle slot was actually less than 50% of the whole object. In an object such as NGC 7009, a single slit position yields only a small cross section through the nebular bright ring. Ideally, if it were not for telescopic observing-time limitations, one would like to secure observations at several spots to get more detailed information about the whole nebula.

5.3. *The Diffuse Radiation Field*

The most elementary approach for the transfer of the diffuse radiation in a spherically symmetric nebula is to reduce the problem to a "local" one. The nebula is assumed to be so optically thick that the diffuse radiation is immediately absorbed locally, i.e., on the spot, without any significant fraction being able to escape. The first attempt at a realistic treatment of diffuse radiation for a spherically symmetrical hydrogenic nebula was made in the series entitled "Physical Processes in Gaseous Nebulae" (see Aller, Baker, & Mendez 1939a, b; Baker, Aller, & Mendez 1939). They calculated the electron temperature T_e from the energy balance equation neglecting collisional excitations of forbidden lines. In the so-called outward-only approach, information from the regions already calculated is used to evaluate an approximation to the diffuse radiation field in the outer region.

Last, the approach used by Harrington and coworkers is to use the above modified OTS or outward-only model as an starting point, and to calculate the intensity of radiation along a network of rays and evaluate J_ν^D correctly. We need to iterate the series of models to secure convergence in this approximation.

Once the stellar radiation field, the density distribution in the nebula, and its chemical composition are given, an initial model is calculated in each model shell (equatorial and polar, respectively) by a modified OTS approximation allowing an outward radiative escape. Next, we follow Harrington in treating the radiative transfer problem in each model shell.

5.3.1. *Formulation for a Model with Spherical Symmetry*

At each radial point r we first start the model calculation with the stellar radiation field mean intensity $J^S(\nu)$ only [set the diffuse radiation field intensity $J^D(\nu)$ equal to zero] and solve for N_e, T_ν, and $N_{e,j}$. We thus can get the emission coefficients for diffuse radiation, $4\pi j(\nu)$, at this point. We iterate to improve the diffuse radiation coefficients. The diffuse radiation field photons, which result from electronic recombina-

tions to the ground state of H I, He I, and He II and to the $n = 2$ level of He II, have mostly $\nu \simeq \nu_0$ and a large absorption coefficient $a_n(\nu)$ near $\nu \simeq \nu_0$, and correspondingly small mean free paths before absorption. We can assume some fraction f of this diffuse radiation to be absorbed on the spot ($f = 1$ for an optically thick nebula and $f = 0$ for an optically thin nebula). For other diffuse sources, namely, the helium lines and the two-photon continuum, however, we allow the radiation to escape outward from the local spot. I used Harrington's method for calculating the escape of the outward radiation and corresponding radiation intensity increase along the tangent rays at the edge of the previous shell (Harrington 1991). With the diffuse radiation J^D and J^S thus obtained, we can recalculate N_e, T_e, and $N_{e,j}$ at the same point and compute new emission coefficients for diffuse radiation. Using a fourth-order Runge-Kutta scheme, the outward integration of the optical depth can also be evaluated from $\kappa(\nu)$. Thus, using the above OTS model solutions as starting point, one can calculate correctly the intensity of radiation (J_ν^D along a network of rays). See Appendix A.

Now we replace the modified OTS solution for $J^d(\nu)$ with the newly obtained diffuse radiation field above in the transfer solutions. In this way, the new solution for $J^D(\nu)$ can be incorporated with the attenuated stellar radiation, to give $J^D(\nu) + J^S(\nu)$, with the aid of which we can evaluate new values of N_e, T_e and $N_{e,j}$ at each radial point. Thus we get new input data for new coefficients for the diffuse radiation. A further iteration might be necessary until $J^D(\nu)$ does not change from one approximation to the next. We chose up to 10 rays through the hollow core inside the nebula ($r < R_c$) in getting the above radiative solutions.

5.3.2. *Formulation for a Composite Shell*

Since a composite model consists of two different density distributions, the above procedures should be applied to equatorial and polar models; the solutions for $J^D(\nu)$ and $\kappa(\nu)$ should be evaluated at various radial shell points of both shell models for the next step. To get a more nearly correct ionization model in our case, however, the radiative transfer problem between the two equatorial and polar shells, resulting in spherically nonsymmetric diffuse radiation solution values of J^D, should be reconsidered. From the emission coefficients and optical depths of the model obtained according to the previous procedure for the spherical case, the solution of the radiative transfer equation for our model can be evaluated by applying the modified Feautrier method.

The necessary steps can be summarized as follows: (1) The nebula is regarded as being made up of many elementary volumes; the line of sight passes through a column of these elementary volumes. (2) We now consider the radiative transfer problem through each column of volume elements along the line of sight. We have to solve the transfer equation via a second-order difference operator involving finite differences, which may be assumed to be continuous except at the boundaries between two shells. We use a spline formula from Hummer, Kunasz, & Kunasz (1973) with some specific boundary conditions for our shell model. (3) In instances where the spline formula sometimes gives improper solutions (i.e., negative values of the radiation field at various points), we employ other numeri-

cal methods to replace these improper radiative transfer solutions. (4) The solutions, which are found for each column of volume elements, however, are stored with the corresponding angular quadrature weight for each radius r in the equatorial and polar shells. Now, the interdependent radiative transfer solutions from two model shells instead of the independent radiative transfer solutions are to be applied to the main program in calculating the ionization structure. (5) The radiative transfer solutions are obtained from the aforementioned four steps, but the solutions are obtained only for the one projection (or inclination) angle, e.g., $i = 90°$ or in the line of sight. Additionally, the radiative transfer problem in the other directions is to be considered also. The repetition of the above four steps for other projection angles is, therefore, necessary to get the correct radiative solutions. The detailed explanations involving the first four steps for the one direction, i.e., in the line of sight, and calculation of the radiation field intensity $J^S + J^D$ are given in Appendix B.

6. THE INFLUENCE OF DUST ON THEORETICAL MODELS

6.1. *Introduction*

The infrared emission by grains provides the most direct evidence for dust in PNs. See, e.g., the discussion by Barlow (1983). Dust-grain absorption in PNs plays a role in two ways. First, it attenuates the radiation flowing radially outward from the PNN. Second, it dims the radiation coming to us along the line of sight; the dust effects on the front and back sides of a nebular gas are not the same. Thus, the weakening of UV resonance lines by internal dust and the thermal emission from dust in PNs should be included in ionization models. Such investigations may supply potentially interesting predictions for IR observers.

The dust/gas ratio, the law of extinction, and the dust size distribution are the essential parameters that must enter into any dust model program. An early attempt to assess effects of dust in PNs employing standard Mie theory, made by Balick (1975), involved an oversimplified dielectric constant dependence. Draine & Lee (1984, 1987) calculated a dielectric function of astronomical silicates ($Mg_{1.1}Fe_{0.9}SiO_4$) and graphites for the optical wavelength range to obtain a dielectric function extending from the far-infrared into the extreme ultraviolet (300 Å–10,000 μm). Theoretical scattering and absorption efficiencies were then calculated with standard Mie theory and dipole approximation for various radii of assumed astronomical silicates and graphites.

The actual nature of the grains may differ from one PN to another (see, e.g., Mathis 1990 for a review). The mechanism of formation will depend on the chemical composition of the progenitor star and the physics of the ejection, which is far from LTE (Rawlings & Williams 1989). Laboratory studies over the range 1300–8000 Å for amorphous silicate smokes, C smoke, and crystalline SiC (Stephens 1980) failed to identify a combination that might explain the extinction function for the interstellar medium (ISM). Apparently SiC is not a major component of the ISM, while the carbonaceous material found in chondritic meteorites appears not to be graphite (Nuth 1985). A possible role of fullerenes remains to be investigated.

The actual shapes of interstellar and circumstellar grains might be extremely irregular, so the whole Mie theory ap-

proach could be too idealized. The absorption properties of these random aggregates (or fractal dust grains) have been studied as a possible source for the wavelength absorption of interstellar dust grains; see Wright (1987). These fractal dust grains, however, cannot yet predict the observed UV properties (in particular the 2200 Å bump).

6.2. *General Effects of Dust Grains on Nebular Spectrum*

Given the appropriate absorption function or functions for the dust grains and assuming a population of grains with a power-law size distribution in the nebula dust model, such as the following,

$$N(a_i) = N_0 a_i^{-p}, \quad a_1 < a_i < a_2 , \qquad (6.1)$$

where $N(a_i)$ is the number density for a grain radius a_i, we may use the equations given by Harrington et al. (1988) to incorporate the role of dust absorption and emission into the nebular theory. As suggested by Mathis, Rumpl, & Nordsieck (1977), p is taken as 3.5. The effective cross section for a spherical grain of radius a is taken from Draine & Lee (1987, Table 1 for graphite and Table 2 for silicates). Also, local external dust may obscure selectively some parts of a source (Harrington, Lutz, & Seaton 1981). Local obscuration by external dust in NGC 7027 is obvious from photographs, e.g., those by Minkowski (reproduced by Aller & Liller 1968).

6.3. *UV Resonance Lines*

Because of the high optical depth in many of the resonance lines, quanta in these lines must travel a much greater distance to escape than does the continuum radiation. Thus radiative trapping can greatly enhance the loss of photon energy through continual scattering and absorption by dust grains, and as a result the dust absorption of resonantly trapped photons and consequent grain heating has been recognized as one of the main sources for the infrared emission from PNs.

Hummer & Kunasz (1980) show that the fraction of photons which escapes is a function of the optical depth due to dust at the line frequency, τ_d. The ratio of the mean path length ($\langle l \rangle$) to the mean optical half-thickness ($T_l/2$) traveled by an escaping line photon in the absence of dust,

$$\rho_0 = \frac{\langle l \rangle}{T_l/2} . \qquad (6.2)$$

Using the resonance line transfer results of Hummer & Kunasz in a plane-parallel slab, Barlow (1983) and Harrington et al. (1988) have calculated the relative heating rates for dust by the resonance lines and by the continuum for NGC 7027 and NGC 3918, respectively. In the Harrington et al. model for NGC 3918, the two sectors are treated as separate, spherically symmetrical nebulae, and the results combined, weighted by their assumed volume fractions.

We also can apply the same treatments for the composite shell at the various impact parameters for a chosen direction. In the grid calculation we can consider the difference between spherical and plane-parallel geometry. Since there are many slabs (each slab consists of many volume elements) in the

model geometry, we first find $\bar{a}_l$ and $\bar{T}_l$ in each column (i) along the line of sight, p_i (see Fig. 9). At the various resonance line frequencies, the corresponding damping constants a_l and line optical depths $\bar{T}_l$ are obtained in the grid along the line of sight, by taking an average weighted by the pertinent density. Thus, a_l and $\bar{T}_l$, which are functions of shell temperature along the line of sight, e.g., $a_l = 2.137 \times 10^{-13} A_{ul} \lambda_0 (\text{Å}) T_\epsilon^{1/2}$ and $T_l = \int \kappa_l \, dr$, where $\kappa_l = 4.2496 \times 10^{-21} B_{lu} \mathcal{N} / T_\epsilon^{1/2}$ for C IV λ1550, are accordingly functions of the position $k = x_i$ (see position x_i in Fig. 2c and resonance line emission zones in Fig. 3),

$$\bar{a}_l|_i = C_a \frac{\int_k a_l \mathcal{N} \, dr}{\int_k \mathcal{N} \, dr}\bigg|_i = C_b \frac{\int_k (\mathcal{N}/T^{1/2}) \, dr}{\int_k \mathcal{N} \, dr}\bigg|_i , \quad (6.3)$$

and, similarly,

$$\bar{T}_l|_i = C_c \int_k \frac{\mathcal{N}}{T_\epsilon^{1/2}} \, dr \bigg|_i , \qquad (6.4)$$

where C_a, C_b, and C_c are constants for each resonance line, $\mathcal{N}$ is the density of an elementary volume in the grid, and A_{ul} and B_{lu} are the Einstein coefficients. We can now find the escape probability f_i ($\simeq e^{-\rho_0 \tau_d}$) using each ρ_0 and τ_d at over the whole projected nebular surface. The values of τ_d along the line of sight at a required frequency can be obtained by employing the trapezoidal rule.

Thus, the intensities I_c of resonance lines, I_c such as the doublet components of the C IV λ1550, C II λ1336, N V λ1240, and Mg II λ2800 which are modified by the dust opacity, can be finally obtained for the model geometry; and the escape probabilities, f_e, can be also given by numerical calculations for each resonance line. Over the whole nebula (or we may
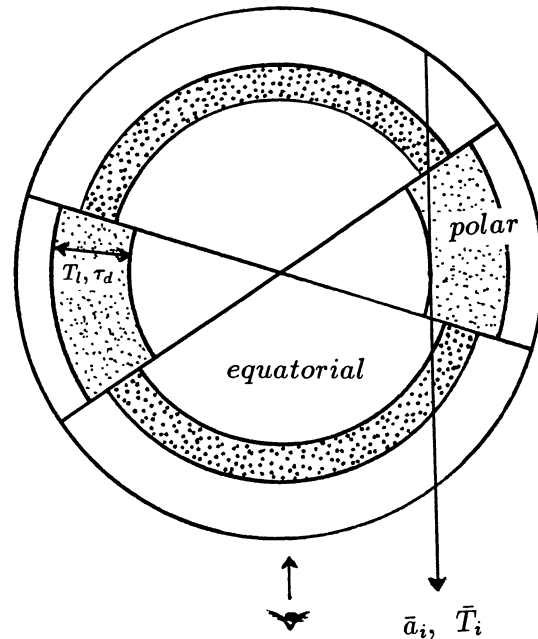

FIG. 3.—UV resonance line treatment. *Dotted area:* resonance line emission zone.

choose the slot area), a resonance line intensity is given as the following summation:

$$I_c = \sum_{i=1}^{n \times n'} I_i(p_i) f_i(p_i) = I_a f_e, \qquad (6.5)$$

where $f_e = I_c/I_a$ is a representative escape probability and $I_a = \sum_{i=1}^{n \times n'} I_i(p_i)$ the resonance line intensity in the absence of dust.

7. MODEL CALCULATIONS

The next step is to apply the model procedure to a real object including all modifications described so far. The static model nebulae constructed for this study postulate statistical equilibrium and do not allow for expansion cooling (adiabatic or shock waves) and departures from a steady state. The dust was assumed to be uniformly mixed with the ionized gas. I assumed a simple radial density variation from the central star out through the PN envelope. The shell density is presumed to decrease radially according to the expression

$$N_H(R) = N_{s_H}/(R_c/R)^a, \quad R > R_c, \qquad (7.1)$$

where R_c is the radial distance from the PNN to the point where the shell density reaches its maximum values, N_{s_H}, or the inner radius of the shell. The parameter a has to be arbitrarily chosen within physically reasonable limits to give the best fit of predicted and observed contours and line spectra. In typical cases, $a = 2$ for density decreasing as the inverse square of the distance from R_c and $a = 0$ for constant density. The inner boundary of the shell is smoothed by a Gaussian density distribution,

$$N_H(R) = N_{0_H} + N_{s_H} \exp\left[-2.773\frac{(R - R_c)^2}{W^2}\right], \quad R < R_c, \qquad (7.2)$$

where W is the full width at half-maximum. A small number density $N_{0_H} = 10$ cm^{-3} is assumed in the hollow core. The Gaussian density variation could also be used to determine the shell width in an idealized shell model; then equation (7.2) would also be assumed to hold for $R > R_c$. In practice, the density variation which has been derived from the observed monochromatic images can be used. If deemed necessary, a filling factor can be introduced to account for voids in the nebular gas distribution.

The calculations of the emission per unit volume from recombination and cascade collisional excitations are straightforward. Also calculated are the mean fractional abundance of an ion, $\langle X_{ij} \rangle$, over nebular volume, and the mean electron temperature $\langle T_{e,ij} \rangle$. See, e.g., Harrington et al. (1988). These mean values are calculated over the entire volume and also over the fractional volume of the entrance slot area.

We first test our procedures on a spherically symmetrical model and compare the result with other "best models" calculated by various workers. After confirming that my model is reasonable, I applied the more elaborate composite model approach to see whether agreement with observations can be improved.

7.1. Basic Parameters

To make predictions for comparison with observations of a particular nebula, in this instance IC 2165, we must adopt a distance, a PNN emergent flux distribution, and a shell mass.

Distance determinations are discussed by various authors: see, e.g., Pottasch et al. (1982), Mendez et al. (1988), and Masson (1989). PNN flux distributions are often taken as Planckian with an effective temperature supplied by some version of a Zanstra (1931) method. Theoretical non-LTE model atmospheres, e.g., Clegg & Middlemass (1987) or Hubeny (1991, 1988; also Hubeny 1992, private communication) have also been employed, but none of these account for the possible modification of emergent flux by emission from a stellar wind.

To illustrate the effects of composition of dust grains on their absorption and emission properties in a PN, we compare a mixture of 50% "astronomical silicates" and 50% graphite, on the one hand, with 100% graphite, on the other. With a C/O abundance ratio ~ 3 we would expect a graphite (or amorphous carbon) composition to be more realistic. The solid particles are assumed to be mixed with the gas with a constant dust-to-gas ratio M_d/M_g in the ionized zone. The minimum and maximum grain radii are 0.001 and 0.15 μm, respectively; they are distributed with a power law of exponent $p = -3.5$ (see eq. [6.1]). The data for silicates and graphites are from Draine & Lee (1987). I have calculated no models for pure silicate dust, although this should be done for O-rich PNs. Additional types of grains are not considered in this study, owing to a lack of available optical data for the extreme-UV region. The main purpose of the dust modeling in this study is to assess a possible effect of internal dust on the nebular UV and optical emissions predictions. Only a small amount of dust ($M_d/M_g = 0.0005$–0.005) was considered in the following ionization model calculation. Thermal emission from a circumnebular dust shell, which could be the major source of the observed IR emission, has not been considered here, since detailed theoretical predictions for the total thermal dust emission from model PNs are outside the scope of this study.

7.2. Comparison of the New Ionization Model with Previous Results

A comparison of present model calculations with those of the Paris-Meudon Observatory workshop and with the old Balick-Keyes program show a generally good agreement with the former (allowing for differences in adopted atomic parameters and number of elements considered) and good accord with the latter for PNs with $T(\text{PNN}) < 50,000$ K. For high-excitation PNs the Balick-Keyes program fails because it does not properly take into account a number of important physical processes.

7.3. IC 2165

Although most PNs do not appear to be spherically symmetrical, they may still show a bilateral symmetry as exhibited in the [N II] $\lambda 6584$ isophotes of this object (Hua & Grundseth 1985). These observers used a telescope of long focal length to secure a sufficient scale for Hα and [N II] $\lambda 6584$ isophotic maps. In spite of a general bilateral symmetry that would permit one to estimate density distributions, there seemed to be

some prominent "blobs" or "condensations." The Hα image exhibits a closed shell, whereas the isophotic contour of the [N II] λ6584 emission varies strikingly through the nebula, showing a toroidal-like structure (east-west direction) reaching a relatively high intensity in the four condensations (see Fig. 5d), whose contours by Hua & Grundseth are compared with theoretical predictions). A density contrast in the equatorial ring and polar conic shells might accommodate such strong condensations in the above isophotic contours.

The distance to IC 2165 seems poorly determined; values range from 1370 pc (Daub 1982) to 5910 pc (Maciel 1985). I have adopted a distance of 2400 pc as determined by Heap et al. (1991). The observed absolute Hβ flux by Heap et al. is $F(H\beta) = 1.288 \times 10^{-11}$ ergs cm^{-2} s^{-1}, and therefore the absolute intrinsic flux is given as 4.94×10^{-11} ergs cm^{-2} s^{-1} using the $E_{B-V} = 0.40$ and corresponding $A_v = 1.24$.

The moderately high excitation nebula IC 2165 is cataloged as having a very faint and very hot PNN. Taking advantage of the superior seeing on Mauna Kea (~0".8), Heap et al. (1991) were able to detect the central star of visual magnitude $m_v = 16.93$. They find a corrected or intrinsic visual magnitude $m_{v_0} = 15.69$ using an adopted $E_{B-V} = 0.40$ and corresponding total extinction $A_v = 3.1 E_{B-V}$. They found Zanstra temperatures of $T_z(H) = 140,000$ K and $T_z(He \, II) = 150,000$ K, while much higher Zanstra temperatures were obtained by earlier studies.

To find the proper PNN atmospheric flux, I carried out an initial model calculation for the spherically symmetrical case with the Clegg et al. (1987) high-temperature non-LTE fluxes, in order to apply the so-called ionic abundance ratio method. Although the plasma diagnostics and ionic concentrations had already been obtained from the observed spectra (in § 3.4), we cannot determine the elemental abundances until the ionic correction factors are found for the unobserved ionic stages. For an initial trial we first used the abundances determined by Aller (1987). The radial variation of the hydrogen density was assumed to be decreasing as the inverse square of the distance from the PNN for the H densities at the inner radial shell, $N_H = 1000, 1500, 2000, \ldots$, up to 7000 cm^{-3}, or assumed to be constant.

The non-LTE atmosphere fluxes for $T_s = 180,000$ K and $T_s = 160,000$ K were interpolated from Clegg et al.'s (1987) H_ν ($4\pi H_\nu = \pi F_\nu$). A number of calculations suggested that it was necessary to truncate the model within the Strömgren sphere radius in order to find the best ionic abundance ratios. We have obtained the following results from such trials: (1) Use of an atmosphere at 180,000 K predicted the He II λ4686 flux to be too strong and that of He I λ5876 to be too weak. Some of the low-excitation lines, e.g., C II λλ2325, 2328 and O II λλ3726, 3729, and other strong emission lines in the next ionization stage, e.g., C IV λλ1548, 1551 and [O III] λλ4959, 5007 were also used to check the ionic abundance ratio. This model gave too high fluxes in both the low-excitation and high-excitation lines. (This result is not due to stratification effects but rather to the character of the atmosphere fluxes, F_ν.) In general predicted and ionic abundance ratios do not agree. (2) Use of an atmosphere at 160,000 K improves the He II λ4686 flux and the He I λ5876 flux, but it still predicts He II λ4686, O II λ3726, and O II λ3729 fluxes that are too high.

On the other hand, the $T_s = 140,000$ K model atmospheres at log $g = 7.0$ and 7.5 reproduce the observed He II fluxes, suggesting that the number of ionizing photons ≥4 rydbergs may be correct. Table 5 presents some of the preliminary model results which have been calculated employing various densities in the nebular shell. The observed line intensities are from the IUE and also from photoelectric spectrophotometry by TPP, and accordingly the predictions [based on the scale of $I(H\beta) = 100$] apply to radiation integrated over the whole nebula. The predictions of columns (4)–(8) are from the truncated spherical nebulae where $I(He \, II \, \lambda4686) \simeq 40$. The mean electron temperature obtained from such a truncation is around the value indicated by the plasma diagnostics diagram (Fig. 1) in § 3.4. The model with a relatively larger inner shell radius $R_{inner} = 0.035$ pc presented in column (4) tends to predict some of the high-excitation line intensities to be too weak (e.g., N V λ1240 and N IV λ1485), and it also tends to predict the low-excitation lines to be too strong (e.g., see C II and C III). In column (8) the filling factor of $\epsilon = 0.5$ is introduced for comparison. All the model predictions in columns (4)–(8) shows a big difference in N V λ1240 and N IV λ1485 fluxes. These lines may have a contribution from the central star. The prediction for the Ne lines is also severely in error. If we adjust the Ne abundance to fit the [Ne III] lines as one might do normally, the predicted [Ne IV] and [Ne V] intensities are too low by a factor of 2 or so. With a much lower density assumed for the nebular shell, the model prediction showed no improvement; it predicted too strong intensities for the low-excitation lines [e.g., $I(C \, II \, \lambda2326) \simeq 150$ from $N_H = 2000$ cm^{-3} with physical parameters $R_{inner} = 0.01$ pc and $R_{cutoff} = 0.077$ pc].

The slot size used in the Hamilton echelle spectroscopy was also considered for the same models as shown in Table 5. The observed line intensities are taken from the Hamilton echelle observations and also from the spatially comparable ITS observations (Aller & Czyzak 1983, 1979). The corresponding predictions for the fluxes in various optical lines at the central region of the nebula are given in Table 6 calculated over a slot size 2".0 × 4".0 rather than 1".16 × 4".0 for reasons explained above.

The aforementioned non-LTE atmosphere at 140,000 K, log $g = 7.5$ is used in these preliminary models. The PNN radius used in the calculations is 0.06 $R_\odot$, and accordingly the stellar luminosity, L_s, is 1420 $L_\odot$. The chosen inner and truncated outer radii are given at the bottom of Table 5. The absolute Hβ flux obtained by the above models was about $F(H\beta) \simeq 1.6 \times 10^{-11}$ ergs cm^{-2} s^{-1}, which is 3 times lower than the observed value. Thus the luminosity of the model atmosphere should be adjusted until the photoionization model reproduces the observed absolute Hβ flux. The assumed density distribution should be adjusted until the model predicts the line intensities and accommodates the limb-to-center contrast in IC 2165 more correctly. In any case, the detailed ionization model should be closely related to a material bounded structure.

Are density contrast models really worth the extra effort involved? Harrington and Clegg's careful investigation of NGC 3918 would indicate that this is certainly true for that particular nebula, and I believe that a similar conclusion is valid for IC 2165. First, I smoothed the contours so that they would corre-

TABLE 5

OBSERVED AND PRELIMINARY MODEL FLUXES FOR THE WHOLE IMAGE OF IC 2165

λ (Å) (1)	ID (2)	I_{obs}[a] (3)	I_{3000} (4)	I_{3000-} (5)	I_{4000} (6)	I_{5000} (7)	I_{5000-} (8)
1240	N v	−(47)	2.0	12.5	14.6	14.2	9.5
1394–1413	O iv]/Si iv	44.1(40)	14.5	18.0	21.5	18.1	18.4
1483/1486	N iv	33(47.4)	17.9	25.5	31.4	32.1	24.1
1548/1551	C iv	1031(975)	1056.7	1338.2	1636	1678.5	1275.6
1640	He ii	260(260)	294	296	304	300	300
1660/1666	O iii]	30.5(33)	39.5	35.6	30.5	30.5	37.7
1747–1754	N iii]	33(37)	35.8	31.4	34.2	33.5	35
1883/1892	Si iii	9.3(3.2)	28.8	22.6	25.4	24.6	25.6
1907/1909	C iii]	943(853)	1236.6	1078.0	1187.3	1159	1229.1
2325/2328	C ii	78(83)	129.9	114.5	108.3	101.5	145.2
2422/2425	[Ne iv]	112(110)	30.6	48.5	56.2	56.3	52.6
3426	[Ne v]	{28}	14.0	29.3	33.48	34.29	25.3
3726/3729	[O ii]	{56}	51.9	49.8	35.6	30.03	47.3
3868	[Ne iii]	{78.5}	193.4	178.0	179.6	178.4	183.4
3969	[Ne iii]	{18.3}	57.8	53.2	53.6	53.2	55.7
4363	[O iii]	{21.4}	19.8	18.6	19.5	19.6	18.5
4471	He i	{4.79}	3.86	3.9	3.89	3.98	3.92
4686	He ii	{41.6}	40.8	38.5	40.32	39.4	40.5
4861	Hβ	100	100	100	100	100	100
4559	[O iii]	{395}	469	440	447	447	436
5007	[O iii]	{1200}	1352.4	1268.6	1288	1289	1257
5755	[N ii]	{0.51}	1.5	1.4	1.03	0.94	1.57
6300	[O i]	{3.55}[b]	0.1	0.1	0.06	0.05	0.12
5876	He i	{11.74}	10.7	10.8	10.9	11.2	11.1
6548/6584	[N ii]	{49}	68.2	68.4	36.22	41.69	40.5
7138	[Ar iii]	{9.55}	13.0	12.3	10.4	10.0	12.53
T_e (K)	...	~14000	13400	13800	14000	13900	13600
PNN: R_s ($R_\odot$)	...	...	0.065	0.065	0.065	0.065	0.065
Shell:							
R_{inner} (pc)	...	...	0.035	0.01	0.01	0.01	0.01
R_{cutoff} (pc)	...	...	0.059	0.055	0.0445	0.0385	0.049
Density: N_H (cm^{-3})	...	...	3000[c]	3000[c]	4000[c]	5000[c]	5000[c]
Filling factor	...	...	1	1	1	1	0.5

NOTE.—All fluxes are given based on the $I(H\beta) = 100$ scale.

[a] Values in parentheses are from Marionni & Harrington 1981. Values in braces are from Torres-Peimbert & Peimbert 1977.

[b] Might be affected by atmosphere.

[c] Radially constant density.

spond to the average of the major and minor axes and adjusted the radial $N(H)$ variation to obtain this mean Hβ profile. The resulting spherically symmetrical model is called model A.

Yet the actual nebula shows a bilateral symmetry, and a realistic model must accommodate this. From an examination of the isophotic maps in Hβ and [N ii] λ6584 by Hua & Grundseth (1985) for the purpose of nebular modeling one may assume N_H(polar cone) ~ $0.5N_H$(equatorial ring), where N_H(polar cone) and N_H(equatorial ring) are respectively hydrogen densities in the polar conical shell and the equatorial ring shells. The relation gives us a general idea of density contrast; the peak hydrogen density of the equatorial shell can be up to twice that of the polar cone (this depends on the exact geometry: size of cone versus equatorial strip). The adopted radial density variations in the equatorial ring and polar cone shells are presented in Figure 4. An inclination angle of $i = 30°$ was also assumed in this density contrast structure to reproduce the elliptical shape in the overall nebular image. In the final model calculation, I used an equatorial angle of $2A = 60°$

(model B); the absolute Hβ flux thus obtained lies close to the observed value. The predicted line intensities from model B are compared with those observed with the large aperture in Table 7 and with the small slot aperture in Table 8, respectively. We centered the slit on the center of the nebula IC 2165, but with the Hamilton echelle spectrograph some image rotation occurs. Therefore, we can choose several different direction angles in the model predictions and average the results to fit the spectra, or simulate effects of image rotation by using a larger slot size in the model calculations, e.g., 2″ × 4″ or even up to 4″ × 4″. Thus a slightly larger slot size of 2″ × 4″ was used to get the predictions in Table 8. Model B gives a much better representation for the Hamilton data than does model A.

Models A and B employed the same physical parameters except for the density variation. The non-LTE atmosphere at 140,000 K, log g = 7.0 is adopted in both models, since it gives a slightly better prediction in He ii fluxes than the log g = 7.5 atmosphere does. The stellar radius adopted was 0.085 $R_\odot$, and the final luminosity of the model atmosphere was 2440 $L_\odot$ at

TABLE 6

OBSERVED AND PRELIMINARY MODEL FLUXES FOR A 2″.0 × 4″.0 SLOT FOR IC 2165

λ (Å) (1)	ID (2)	I_{obs}[a] (3)	I_{3000} (4)	I_{3000-} (5)	I_{4000} (6)	I_{5000} (7)	I_{5000-} (8)
3726	[O II]	18.39	27.4	16.1	12.1	11.4	18.2
3729	[O II]	9.35	14.1	8.3	5.8	5.2	8.2
3868	[Ne III]	79.6(95.5)	176.6	109.7	110.9	117.9	121.1
3969	[Ne III]	25.8(28.2)	52.7	32.8	33.9	35.2	36.2
4267	C II	0.33	0.45	0.28	0.28	0.29	0.33
4363	[O III]	19.9	19.94	15.29	16.34	17.47	16.29
4471	He I	2.8	3.22	2.35	2.36	2.57	2.43
4686	He II	63.5(61.7)	52.4	68.7	68.1	64.86	67.98
4712	[Ar IV]	5.3(7.1)	10.4	7.3	7.5	7.7	7.2
4725	[Ne IV]	0.688	0.27	0.36	0.39	0.41	0.40
4727	[Ne IV]	0.64	0.24	0.32	0.35	0.36	0.35
4741	[Ar IV]	5.9(6.2)	10.1	7.08	7.98	8.74	8.20
4959	[O III]	369(398)	454	328	345	367	351
5007	[O III]	1158	1309	946.4	994	1058	1011
5537	[Cl III]	0.36(0.3)	0.54	0.36	0.36	0.38	0.43
5755	[N II]	0.47(0.5)	1.15	0.67	0.53	0.54	0.91
5876	He I	7.75(7.2)	9.09	6.71	6.74	5.62	6.93
6300	[O I]	1.1[a]	0.07	0.05	0.03	0.03	0.07
6312	[S III]	1.33	1.09	0.66	0.61	0.63	0.78
6437	[Ar V]	1.36	1.20	1.96	2.06	2.03	1.96
6548	[N II]	5.9	13.4	8.0	6.1	6.0	10.4
6563	Hα	286	289.9	292.3	292.3	292.8	290.3
6584	[N II]	17.5	38.8	23.2	17.7	17.4	30.1
6717	[S II]	0.88	0.81	0.49	0.32	0.28	0.47
6730	[S II]	1.37	1.31	0.78	0.55	0.50	0.85
7008	[Ar V]	2.12	2.59	4.23	4.45	4.39	4.23
7138	[Ar III]	7.28	10.2	6.19	5.58	5.74	7.14
7320	[O II]	1.16	2.10	1.27	1.15	1.24	1.91
7330	[O II]	0.98	1.68	1.01	0.91	0.99	1.53
7751	[Ar III]	1.54	2.47	1.50	1.36	1.39	1.73
8048	[Cl IV]	0.75	0.95	0.71	0.76	0.82	0.75
9072	[S III]	5.25	13.56	8.26	7.60	7.82	9.75
9535	[S III]	20.1	33.1	20.15	18.6	19.1	23.8
Density N_H (cm^{-3})	...	...	3000[1][b]	3000[1][b]	4000[1][b]	5000[1][b]	5000[0.5][b]

NOTE.—Physical parameters used in models are the same as in Table 5.
[a] Values in parentheses are from Aller & Czyzak 1983, 1979.
[b] Values in brackets are filling factors.

the adopted distance of 2400 pc. With this stellar luminosity the observed absolute Hβ flux could be reproduced, and the predictions over the whole nebula are presented in Table 7. One may improve the predictions slightly in some lines with a little different hydrogen radial density variation using the method employed in model A. However, it seems unlikely to yield more satisfactory predictions of line intensities, while the predictions of model B show better agreement with the observations than do those of model A.

The Hβ and [N II] λ6584 maps from this final model B are shown in Figures 5a and 5c and compared with those of Hua & Grundseth (1985) in Figures 5b and 5d. Although the prediction cannot reproduce observed irregularities such as the small symmetrical blobs in the [N II] image, the overall shape, limb-to-center contrast, and nebular physical size produced by the final model seem to fit the pattern of the observed isophotes fairly well.

Using ultraviolet-blue-visual (*UBV*) filter curves (e.g., Hayes & Latham 1975), the dereddened apparent magnitudes
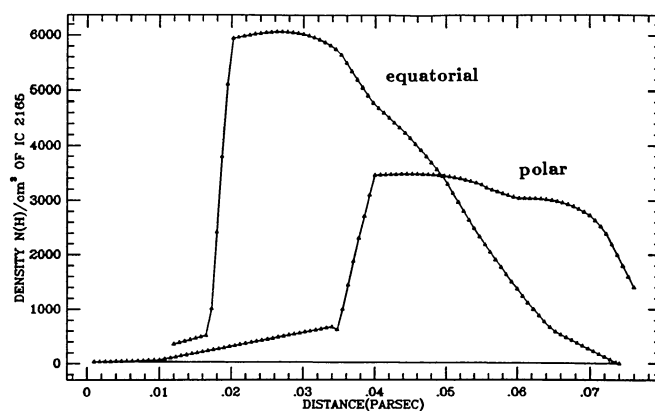

FIG. 4.—Radial density variations of IC 2165 (model B)

TABLE 7
Total or Large-Aperture Line Fluxes for IC 2165

λ (Å) (1)	ID (2)	I_{obs}[a] (3)	$I_{model\ A}$ (4)	$I_{model\ B}$[b] (5)
Hβ₀ (ergs s⁻¹ cm⁻²)	...	4.94×10^{-11}	3.5×10^{-11}	4.70×10^{-11}
5 GHz flux (Jy)	...	...	0.186	0.167
1240	N v	−(47)	41.6	13.0[13.7]
1394–1413	O iv]/Si iv	44(40)	29.3	18.4[20.0]
1483/1486	N iv	33(47.4)	61.4	37.8[41.8]
1548/1551	C iv	1031(975)	1815.5	1188.9[1296]
1640	He ii	260(260)	281.3	239[254.3]
1660/1666	O iii]	30.5(33)	56.4	51.6[55.1]
1747–1754	N iii]	33(37)	42.6	46.6[48.6]
1883/1892	Si iii]	9.3(3.2)	11.1	12.8[12.9]
1907/1909	C iii]	943(853)	870.8	959.4[954.4]
2325/2328	C ii	78(83)	43.7	81.4[75.2]
2422/2425	[Ne iv]	112(110)	52.8	44.9[40.4]
2796/2804	Mg ii	3.7(6.1)	4.4	7.5[7.3]
3426	[Ne v]	{28}	37.6	21.2[20.0]
3728/3726	[O ii]	{56.2}	21.4	43.6[43.0]
3868	[Ne iii]	{78.5}[100]	129.8	144.7[144.6]
3969	[Ne iii]	{18}[30]	38.8	43.3[43.3]
4102	Hδ	{26.9}	25.1	25.1[25.0]
4340	Hγ	{46.8}	45.9	45.9[45.6]
4363	[O iii]	{21.4}	23.95	23.20[22.87]
4471	He i	{4.79}	3.74	4.17[4.20]
4686	He ii	{41.6}	43.6	37.2[36]
4861	Hβ	{100}	100	100[100]
5007	[O iii]	{1202}	1233	1260[1259]
5755	[N ii]	{0.51}	0.50	1.33[1.32]
5876	He i	{11.7}	10.51	11.87[12.07]
6300	[O i]	{3.55}	0.01	0.08[0.07]
6312	[S iii]	{1.86}	0.78	1.29[1.29]
6563	Hα	{276}	303.1	307.2[308.1]
6548/6584	[N ii]	{49}	19.4	53.1[52.7]
6678	He i	{3.39}	2.52	2.86[2.91]
6717/6730	[S ii]	{6.76}	1.1	2.78[2.75]
7136	[Ar iv]	{9.55}	4.80	8.55[8.64]
7320/7330	[O ii]	{6.92}	1.85	4.45[4.43]

[a] Observed intensities given in braces are from Torres-Peimbert & Peimbert 1977; those given in brackets are from Kaler, Czyzak, & Aller 1968.

[b] Values in brackets obtained using graphite grains only.

at U, B, V can be calculated from the adopted model atmosphere fluxes. The subroutine program which has been used to get an apparent UBV magnitude is originally due to Harrington (1991). The above choice of stellar luminosity and temperature gives an apparent visual magnitude consistent with the observations by Heap et al. (1991). The predicted dereddened apparent magnitude $m_v \simeq 15.89$ mag obtained in the final model was a 0.2 mag lower than the observation, 15.69 mag. To predict the resonance line fluxes correctly, e.g., C iv λ1550, a dust-to-gas ratio $M_d/M_g = 0.005$ was assumed in all the above models. This amount of the dust grains could destroy the UV resonance lines up to 20%. The predicted intensities in the brackets of column (5) in Tables 7 and 8 are calculated from the model where only graphite grains are used in the nebular gas. The effects are largest for C iv (∼10%) but are relatively small for most other lines.

The calculated mean electron densities from the final model B were 3770 cm⁻³ for the whole nebula and 3,930 cm⁻³ for a 4″ × 2″ entrance. The final model is calculated from 140,000

K, log g = 7.0. Non-LTE atmospheric fluxes give a higher electron temperature than does the log g = 7.5 atmosphere (∼500 K difference); thus the predicted electron temperatures calculated with the log g = 7.5 atmosphere are closer to those estimated by the plasma diagnostics. The mean excitation temperatures ($\langle T_e \rangle$) from the final model were 15,000 K for the whole nebula and 16,000 K for the 4″ × 2″ entrance. I did not apply the mean temperatures for each ion derived from the final model B to redefine the fractional ionic concentration. The mean electron temperatures for each ion from a slot observation are expected to be higher than those from a large-aperture observation. Our calculation shows that the mean temperatures from a central slot are slightly higher than for the integrated light in the low-excitation lines, and up to 450 K higher in the high-excitation lines.

To find the chemical abundances, it is necessary to calculate from a model the ionization correction factors (ICFs) for the ionization stages which are not observed. From model B the fractional ionic abundances are obtained for the whole nebula,

TABLE 8

LINE FLUXES WITH SMALL APERTURE IN CENTER OF IC 2165

λ (Å) (1)	ID (2)	I_{obs}[a] (3)	$I_{model A}$ (4)	$I_{model B}$[b] (5)
3347	[Ne v]	17.9	33.0	18.8[18.1]
3424	[Ne v]	35.2	90.5	51.6[49.7]
3722	H14+[S III]	2.85	2.15	2.45[2.45]
3726	[O II]	18.39(22.4)	4.4	18.6[18.4]
3729	[O II]	9.35(13.8)	2.4	9.9[9.8]
3868	[Ne III]	85.7(95.5)	55.8	98.0[98.6]
3969	[Ne III]	25.8(28.2)	16.7	29.3[29.5]
4068	[S II]	0.87	0.06	0.30[0.30]
4076	[S II]	0.71	0.02	0.10[0.10]
4164	[K v]	0.14	0.16	0.17[0.16]
4267	C II	0.33(0.41)	0.09	0.17[0.17]
4363	[O III]	20.74(19.1)	16.83	20.28[20.18]
4471	He I	2.81(2.51)	1.73	2.52[2.55]
4686	He II	63.5(61.7)	80.46	66.22[65.18]
4712	[Ar IV]+[c]	5.9(6.2)	0.15	6.45[6.47]
4725	[Ne IV]	0.69	0.54	0.46[0.45]
4727	[Ne IV]	0.64	0.47	0.41[0.40]
4741	[Ar IV]+[c]	5.9(6.2)	5.27	6.56[6.59]
4959	[O III]	369(398)	261	350[352]
5007	[O III]	1158(1175)	754	1009[1015]
5193	[Ar III]	0.106(0.10)	0.02	0.07[0.08]
5198	[N I]	0.16	0.004	0.01[0.01]
5200	[N I]	0.11	0.04	0.01[0.01]
5310	[Ca v]	0.12(0.09)	0.13	0.14[0.14]
5325	[Cl IV]	0.068(0.05)	0.04	0.05[0.05]
5517	[Cl III]	0.328(0.26)	0.15	0.31[0.32]
5537	[Cl III]	0.36(0.30)	0.17	0.37[0.38]
5755	[N II]	0.47(0.48)	0.18	0.88[0.88]
5876	He I	7.64(7.24)	3.22	7.15[7.29]
6103	[K IV]	0.322(0.21)	0.21	0.31[0.31]
6300	[O I]+[d]	1.20(1.15)	0.004	0.05[0.05]
6312	[S III]+[c]	1.32	0.35	0.90[0.90]
6363	[O I]	0.44(0.36)	0.004	0.02[0.02]
6437	[Ar v]	1.32(0.55)	1.85	1.56[1.54]
6548	[N II]	5.36(6.03)	1.7	8.9[8.8]
6563	Hα	282.8(281.8)	309.8	304.9[306.1]
6584	[N II]	17.12(19.95)	4.8	25.7[25.6]
6678	He I	1.71(1.86)	1.08	1.70[1.73]
6717	[S II]	0.86(0.91)	0.13	0.70[0.70]
6730	[S II]	1.34(1.55)	0.20	1.09[1.08]
7008	[Ar v]	2.07(6.76)	4.01	3.36[3.34]
7138	[Ar III]	7.12(6.76)	1.54	5.15[5.22]
7172	[Ar IV]	0.31	0.09	0.10[0.10]
7239	[Ar IV]	0.26(0.20)	0.06	0.07[0.08]
7265	[Ar IV]	0.23(0.19)	0.07	0.08[0.08]
7320	[O II]	1.14	0.44	1.61[1.61]
7330	[O II]	0.96	0.34	1.29[1.29]
7532	[Cl IV]	0.35	0.24	0.29[0.30]
7751	[Ar III]	1.50(1.95)	0.38	1.25[1.27]
8048	[Cl IV]	0.73(0.78)	0.55	0.68[0.69]
8581	[Cl II]?	0.022	0.01	0.06[0.06]
9072	[S III]	6.0	3.54	9.60[9.72]
9535	[S III]	20.4	8.66	23.44[23.78]

NOTE.—All fluxes are given based on the $I(H\beta) = 100$ scale. Physical parameters used in models are the same as in Table 7. A slightly larger slot size of models was used: 2″ × 4″. Slit position is centered at the PNN: (0″.0, 0″.0).

[a] Observed intensities given in parentheses are from Aller & Czyzak 1983, 1979.

[b] Values in brackets obtained using graphite grains only.

[c] Drip correction is done for this line.

[d] Might be affected by atmosphere.

and the normalized values for each element are given in Table 9. Since the Hamilton echelle spectrograph data in the optical region were secured over a small portion of the nebular central region, the corresponding fractional ionic abundances should also be determined for a small slot; these are given in Table 10. Since the ionic concentrations of O, S, Ar, Cl, Ca, and K are mostly determined from the Hamilton data, for these elements it is necessary to determine the ICFs from Table 10, whereas the ICFs for C, Ne, and Si come from Table 9. Table 11 gives the final abundance determinations. Column (2) lists the sum of the ionic concentrations derived in Table 4 (col. [7]). Column (3) lists the ICFs from model B. Column (4) gives abundances on the scale $N(H) = 1.0$, which is calculated by multiplying the entries in column (2) by the ICFs in column (3). Column (5) gives the abundance actually employed in model B. Column (6) gives $\Delta = [\log N(\text{ICF method}) - \log N(\text{model})]$. The seventh column gives the previous estimation by Aller (1987).

The helium abundance is about the same in both Aller's and the present determinations. The carbon abundance by the current study shows a large difference. Aller estimated $N(C)/N(H) = 8.3 \times 10^{-4}$, while I obtain $\sim 4.2 \times 10^{-4}$. Also Ne and Ar abundances show a factor of 2 difference between two studies.

Model A results are not used in this investigation. Since model A was finally discarded, I did not try to refine it to get the correct absolute Hβ flux. The line predictions from model A are also presented in Tables 7 and 8 for comparison, however. In summary, the two-component model B appears to be superior to model A, where the density distribution was derived empirically from the smoothed isophotes and spherical symmetry was assumed.

8. CONCLUSIONS AND SUGGESTIONS

The most realistic emerging models of PNs envisage them in the framework of an evolutionary process (Kwok, Purton, & FitzGerald 1978; Balick 1987; Mellema, Eulderink, & Icke 1991; Icke, Balick, & Frank 1992). The basic concept seems to be that a star in the mass range 0.5–5 $M_\odot$ ascends the asymptotic giant branch (AGB) and loses its outer envelope. In the first phase, mass is lost in a slow-moving dense wind that is not spherically symmetrical. Ejection depends on latitude in such a way that far more material is lost in equatorial than in polar regions. Nearly all of the actual mass loss occurs at this phase. Later, there follows a fast spherically symmetrical wind ($V \sim$ 1000–3000 km s^{-1}) that impinges upon the relatively massive slow-moving previously detached envelope. The recent work of Balick and his coworkers has shown that the hydrodynamical effects of the confrontation between these two winds produces nebular morphologies that can be identified with what we actually observe. The common elliptical and more spectacular butterfly structures (which show jetlike forms indicating strong collimation inside the bubble) are products of differing density patterns in the slow red giant wind. Numerical modeling of the early evolution of aspheric PNs (Icke et al. 1992) has shown how reasonable mass distributions in the AGB envelope can produce a variety of nebular forms.

A non–spherically symmetrical model has been accepted here. A comparison of the fluxes calculated from columns
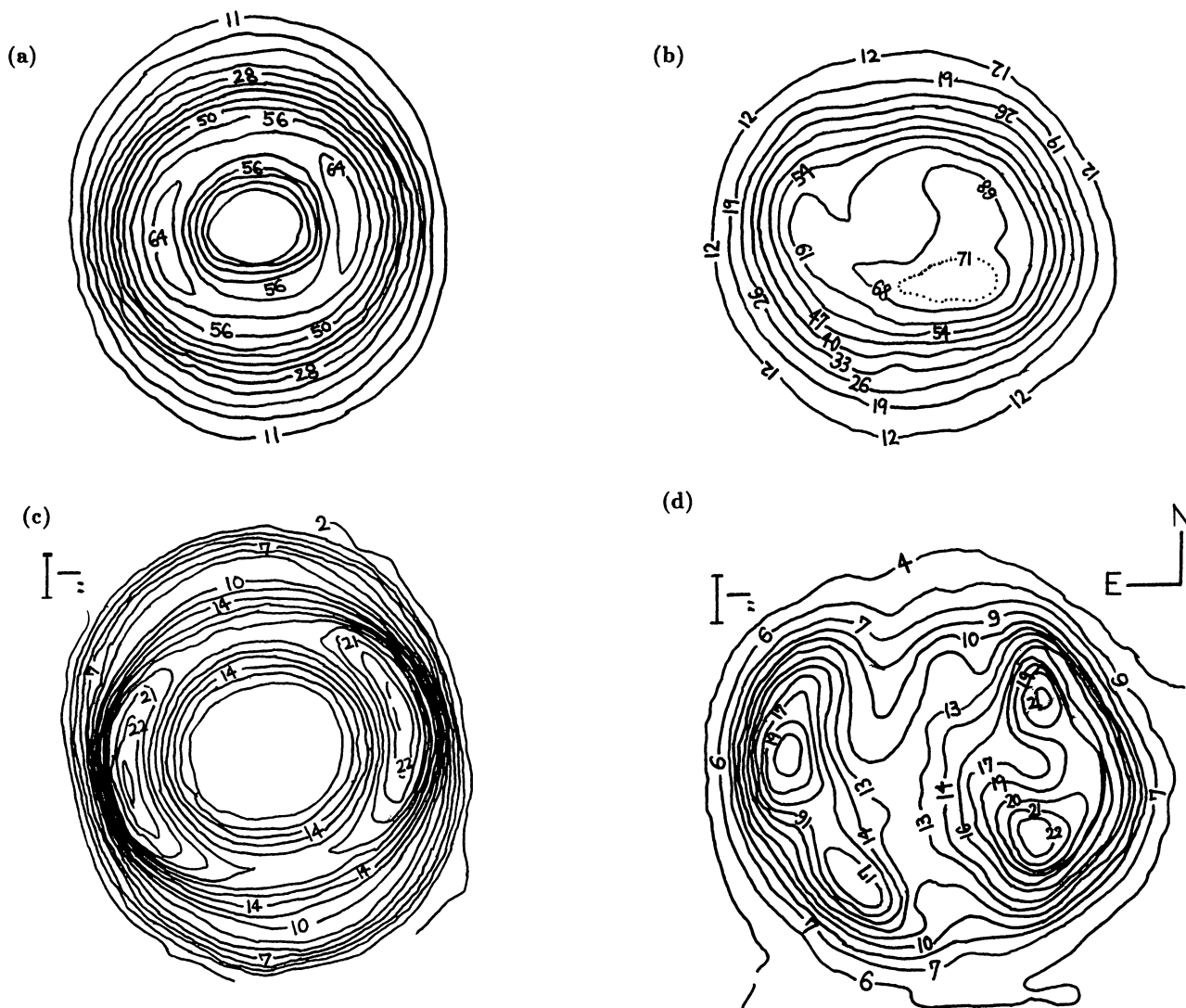
(a)

(b)

(c)

(d)

N

E

FIG. 5.—Surface brightness contours from model B (inclination $i = 30°$) and processed images from narrow bandpass interference filters ($\Delta 5.5$ Å) from Hua & Grundseth (1985): (a) theoretical isophotic contour in Hβ; (b) processed images centered on Hα; (c) theoretical isophotic contour in [N II] $\lambda6584$; (d) processed images centered on [N II] $\lambda6583$. Four strong condensations are shown in [N II] isophotes in (d) (but not predicted in [c] by model B).

taken through the nebula for the spherically symmetrical and "ring plus cone" model shows the superiority of the latter. The present models are static structures. Ideally, in the spirit of suggestions by Harrington & Marionni (1976) and of Tylenda (1979), we should consider time-dependent effects, but these only become important when relaxation times for atomic processes become comparable to expansion rates.

In a limited area of the image, it is possible to measure the line profiles and draw some conclusions about the nebular velocity field. Doppler-shifted double peaks, which are caused by directional shell expansions, exist in the spectra of IC 2165 and Hu 1-2 and in other PNs as well. At this stage of modeling development, we can only include a simple velocity field in the shell of a PN. Assuming a simple expansion velocity for the shell, I obtained some preliminary results, which could reproduce the observed line profiles from the current nebular model for IC 2165. A detailed modeling procedure involving possible

TABLE 9

FRACTIONAL IONIC ABUNDANCES OF IC 2165 FOR A LARGE SLOT OVER WHOLE NEBULA

Element	I	II	III	IV	V	VI
H	0.007	0.993	...	...	...	...
He	0.002	0.751	0.249	...	...	...
C	0.000	0.074	0.623	0.253	0.049	0.000
N	0.000	0.061	0.629	0.286	0.020	0.004
O	0.000	0.049	0.846	0.090	0.013	0.002
Ne	0.000	0.009	0.784	0.144	0.048	0.014
S	0.000	0.023	0.392	0.502	0.058	0.022
Ar	0.000	0.023	0.392	0.459	0.066	0.035
Cl	0.002	0.067	0.356	0.372	0.174	0.022
Ca	0.000	0.025	0.166	0.585	0.133	0.072
Mg	0.000	0.089	0.685	0.135	0.065	0.026
F	0.000	0.006	0.632	0.233	0.109	0.061
K	0.000	0.004	0.051	0.743	0.129	0.042
Si	0.000	0.365	0.229	0.194	0.168	0.042

TABLE 10

FRACTIONAL IONIC ABUNDANCES OF IC 2165 FOR A SMALL ENTRANCE
SLOT OBSERVATION CENTERED AT PNN

Element	I	II	III	IV	V	VI
H	0.008	0.992	...	...	...	...
He	0.002	0.586	0.414	...	...	...
C	0.000	0.060	0.549	0.281	0.110	0.000
N	0.000	0.049	0.562	0.332	0.044	0.012
O	0.000	0.039	0.742	0.179	0.032	0.006
Ne	0.000	0.007	0.632	0.224	0.099	0.035
S	0.000	0.018	0.319	0.512	0.088	0.050
Ar	0.000	0.002	0.332	0.444	0.120	0.080
Cl	0.002	0.054	0.290	0.340	0.245	0.049
Ca	0.000	0.007	0.345	0.305	0.268	0.070
Mg	0.000	0.068	0.551	0.195	0.124	0.060
F	0.000	0.005	0.469	0.288	0.196	0.037
K	0.000	0.003	0.041	0.595	0.204	0.123
Si	0.000	0.280	0.199	0.196	0.242	0.077

hydrodynamic flow in the nebulae might be necessary to study the line profiles correctly. Such an extensive program lies outside the scope of the present investigation.

How well it reproduces the nebular spectrum is, of course, one of the crucial tests of a model. Although PN models based on currently available theoretical stellar fluxes can predict He II $\lambda 4686$ in high-excitation objects, currently [Ne v] presents a problem. To remove this discordance, it might be necessary to alter the shape of the flux distribution in the high-energy region such that a larger fraction of the energy between 4.6 and 7 rydbergs was emitted at higher frequencies, which would allow a larger fraction of high-ionization stages in the nebula. Adam & Köppen (1985) proposed that the stellar wind of the PNN in NGC 1535 could affect the ionizing continuum absorbed by the nebula. In this approach, the total number of photons emitted would have to be kept constant in order not to affect the He II fluxes. Since the ionization threshold potential of Ne III is relatively higher than that of most other elements for the same ionization stages, this would not seriously affect the prediction in other lines. Hubeny's stellar atmosphere might im-

prove this situation, since his model atmosphere can include the abundance contributions of Ne and other elements. Using the available Hubeny (1992) model atmospheres, I was unable to improve the results for [Ne v] and [Ne III] for NGC 7027.

Since we cannot fully understand the nebular plasma diagnostics and the stratification effects without knowing the correct geometry, it is important to consider a fully three-dimensional density distribution even for spherically symmetrical objects. Along with improvements in observational techniques, more realistic ionization models should be developed to explain both the spectra and shapes of PNs with appropriate density distributions in the nebular shell(s). It has to be emphasized that it is impossible to choose the density variation and the shape independently to model the nebula appropriately. The final model for IC 2165 is somewhat similar to a prolate ellipsoidal spheroid. The preferred geometry for NGC 7027 and NGC 7009 was a highly flattened disklike structure, but in this study I did not arrive at any final conclusion on the geometry of these particular objects. IC 2165 and NGC 7009 might be material-bounded nebulae, but NGC 7027 is most likely interpreted as an ionization-bounded (i.e., radiation-bounded) structure.

The current model is based on stationary flows in nebular shells occurring in the assumed PN evolutionary history. A more detailed hydrodynamical flow model eventually should be introduced in grid modeling procedures to account for the morphology and kinematics of other somewhat complicated nebulae. By expanding model calculation techniques to include the circumstance that different bodies of observational data refer to different things (total nebular fluxes or pencils taken through various parts of the image), and by noting that most nebulae are not spherically symmetrical shells, improved nebular chemical compositions may be obtained.

TABLE 11

IONIC CONCENTRATIONS: IC 2165

Element (1)	$\Sigma[N(i)/N(H^+)]$ (2)	ICF (3)	ICF Method (4)	Model (5)	Δ (6)	ICF Method[a] (7)	Δ[a] (8)
He	0.1073	1.00	0.1073	0.105	...	0.104	...
C[b]	4.08E−04	1.05	4.28E−4	4.10E−4	0.02	8.30E−4	0.04
N	6.33E−05	1.00	6.33E−5	8.00E−5	−0.10	1.07E−4	0.10
O	1.37E−04	1.04	1.42E−4	2.00E−4	−0.15	2.60E−4	0.04
Ne[b]	5.95E−05	1.08	6.43E−5	5.00E−5	0.11	8.90E−5	0.02
Si[b]	4.08E−07	4.37	1.78E−6	3.00E−6	0.48	...	...
S	2.00E−06	1.18	2.36E−6	2.80E−6	−0.07	2.60E−6	0.10
Cl	5.52E−08	1.59	8.78E−8	9.00E−8	−0.01	1.40E−7	0.08
Ar	8.25E−07	1.49	1.23E−6	1.00E−6	0.09	2.00E−6	0.12
K	5.61E−08	1.25	7.01E−8	8.00E−8	−0.06	6.00E−8	0
Ca	3.11E−08	3.73	1.16E−7	1.20E−7	−0.01	9.00E−8	0.13

[a] Previous estimation by Aller 1987.
[b] The ICFs for these elements pertain to the whole nebular image.

APPENDIX A
RADIATIVE TRANSFER SOLUTION WITH SPHERICAL SYMMETRY

In a spherically symmetrical nebula with a central hollow and adopted inner radius R_c and an outer radius R, the radiation intensity of frequency v depends on the radial distance r from the center and the angle θ between the radiation direction and the outwardly directed radius vector at that point, as follows:

$$\frac{dI_\nu(r, \theta)}{ds} = \frac{\partial}{\partial r} I_\nu(r, \theta) \frac{dr}{ds} + \frac{\partial}{\partial \theta} I_\nu(r, \theta) \frac{d\theta}{ds} = -\kappa_\nu(r)[I_\nu(r, \theta) - S_\nu(r)], \quad R_c \leq r \leq R , \tag{A1}$$

where $dr/ds = \cos \theta$, and $d\theta/ds = -(\sin \theta)/r$ (Fig. 6a). Since both $\kappa_\nu(r)$ and $S_\nu(r)$ [$\equiv j_\nu(r)/\kappa_\nu(r)$] have already been obtained in the main program, we can find $I_\nu(r, \theta)$ by solving the radiative equation in the suggested nebular geometry. Now the values of the moments $J_\nu(r)$, $H_\nu(r)$, and $K_\nu(r)$ are defined as the values for $m = 0, 1, 2$, respectively, of the integral

$$\int_0^{4\pi} dw \, I_\nu(r, \mu, \psi)/4\pi = \int_{-1}^{1} \int_0^{2\pi} d\mu \, \mu^m d\psi \, I_\nu(r, \mu) \bigg/ \int_{-1}^{1} \int_0^{2\pi} d\mu \, d\psi$$

$$= \int_0^1 d\mu \, \mu^m I_\nu(r, \mu) \bigg/ \int_0^1 d\mu , \tag{A2}$$

where $\mu = \cos \theta$ and $\int_0^{2\pi} d\psi = 2\pi$. We drop the subscript ν in the source function S_ν, opacity κ_ν (or optical depth τ_ν), and radiation intensity I_ν for simplicity. We can simplify the radiative transfer equation using a system of cylindrical coordinates (the Feautrier method as discussed by Hummer et al. 1973).

We choose rays tangent to each shell (r), and use values $p = r \sin \theta$ for the impact parameter and $x = (r^2 - p^2)^{1/2}$ in the cylindrical coordinates (p, x), so the optical depth variables from the back to the front on a line of constant p can be simplified as

$$d\tau(p) = \kappa(r)dx(p), \qquad 0 \leq \tau(p) \leq \tau_{max} \, [= 2\tau_n(p)] , \tag{A3}$$

with $\tau(p) = 0$ at $x = -(R^2 - p^2)^{1/2}$ and $\tau(p) = \tau_n(p) = 2\tau_n(p)$ at $x = (R^2 - p^2)^{1/2}$. Therefore, the transfer equation can be written as

$$dI^\pm(p, \tau)/dr = \pm[S(r) - I^\pm(p, \tau)] , \tag{A4}$$

where I^+ and I^- refer to radiation flowing forward and backward to the observer, respectively. Since the core is assumed to be hollow, $\kappa(r) = 0$ for $r < R_c$. The absence of radiation falling on the outer surface at the outer radius of a PN gives the special boundary conditions $I^+(p, 0) = 0$ and $I^-(p, 2\tau_n) = 0$. In the middle of a cylindrical cross section, we also set the second boundary condition as $I^-(p, \tau) = I^+(p, \tau)$.
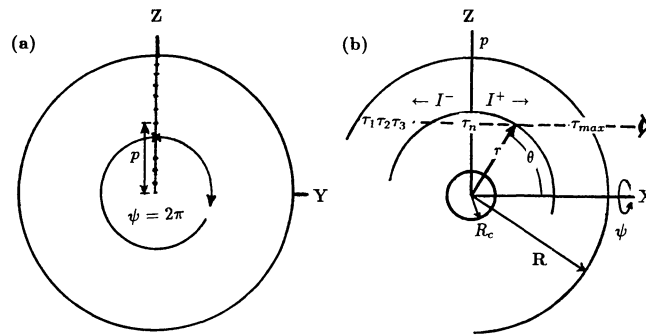

FIG. 6.—Definitions of geometrical variables. (a) Radial shell R, a spherically symmetrical radial shell R in the sky, i.e., an observer is above the (y, z)-plane. (b) Cross section; θ is the angle between a radius vector r and a line of sight.

By introducing the following two dependent variables to solve the radiative equation, $U(p, \tau) = \frac{1}{2}[I^+(p, \tau) + I^-(p, \tau)]$ and $V(p, \tau) = \frac{1}{2}[I^+(p, \tau) - I^-(p, \tau)]$, we can have a second derivative equation from the transfer equation (A4) on a line of constant p that is expressed only in terms of U. The second derivative, which is to be solved from the source function $S(r)$ on each impact parameter p with the boundary conditions, is

$$d^2U(p, \tau)/d\tau^2 = U(p, \tau) - S(r) . \tag{A5}$$

It is easy to show that $dU(p, \tau)/d\tau = -V(p, \tau) = -\frac{1}{2}[I^+(p, \tau) - I^-(p, \tau)]$. The boundary conditions for the cross sections become at the outer surface of the nebular model sphere, $r = R$,

$$dU(p, \tau)/d\tau - U(p, \tau) = -\tfrac{1}{2}[I^+(p, \tau) - I^-(p, \tau)] - \tfrac{1}{2}[I^+(p, \tau) + I^-(p, \tau)] = 0, \qquad \tau = 0 , \tag{A6}$$

where $I^+(p, 0) = 0$, and

$$dU(p, \tau)/d\tau + U(p, \tau) = -\tfrac{1}{2}[I^+(p, \tau) - I^-(p, \tau)] + \tfrac{1}{2}[I^+(p, \tau) + I^-(p, \tau)] = 0, \qquad \tau = 2\tau_n(p) , \tag{A7}$$

where $I^-(p, 2\tau_n) = 0$ (see Fig. 6b). In fact, these two boundary conditions at $\tau = 0$ and $\tau = 2\tau_n(p)$ are the same one (because of spherical symmetry). The other true second boundary condition in the middle point ($x = 0$ in Fig. 6b) is

$$dU(p, \tau)/d\tau \ [= V(p, \tau)] = 0, \qquad \tau = \tau_c(p) , \tag{A8}$$

where $I^-(p, \tau) = I^+(p, \tau)$ at $\tau_c = \tau_n(p)$. Due to the spherical symmetry of the considered PN, we may further be able to ignore the backward half–cross section (where $x < 0$) in the above equations and correspondingly recondition the optical depth variables, $\tau = \tau_c = 0$ at $x = 0$ and $\tau = \tau_n(p)$ at $x = R$, to solve the boundary equations. The detailed spline formulae for the spherically symmetrical case are given by Hummer et al. (1973). Instead of finding the values of U from the two boundary equations, however, we may employ the following formulae (Harrington 1991) for I^+_k and I^-_k:

$$I^+_k = I^+_{k-1}e^{-h_k} + S_k(1 - e^{-h_k}) + (S_{k-1} - S_k)\left[\frac{1 - e^{-h_k}(1 + h_k)}{h_k}\right] \tag{A9}$$

and

$$I^b_{k'} = I^b_{k'-1}e^{-h_{k'}} + S^b_{k'}(1 - e^{-h_{k'}}) + (S^b_{k'-1} - S^b_{k'})\left[\frac{1 - e^{-h_{k'}}(1 + h_{k'})}{h_{k'}}\right], \tag{A10}$$

where $h_k = h_k(p) = \tau_k(p) - \tau_{k-1}(p)$ can be evaluated by the trapezoidal rule, and $k' = n + 1 - k$.

Although the radiative transfer problem has to be solved along the line of sight (various points x_k) for each p in a spherical object, the arrays of solutions can be stored for shell radius r with the angular quadrature weights (instead of storing them for each p). Therefore, to evaluate the moment integral for fixed radial shell r, we use the quadrature sums for $J(r)$ (our interest is $m = 0$ in eq. [A2]), as

$$J^d(r) = \int_a^b U \, d\mu \Big/ \int_a^b d\mu \cong \sum_{i=1}^L U_i \Delta\mu_i \Big/ \sum_{i=1}^L \Delta\mu_i , \tag{A11}$$

where the angular quadrature weight $\Delta\mu_i$ is obtained by trapezoidal rule in a schematic way. Since it is spherical symmetry, the integration of the above equation is to be done basically from $a = 0$ to $b = 1$. L in the above equation is determined by the impact parameters that are chosen at points tangent to the radial shells. The formulae for finding the angular quadrature weights are given by Hummer et al. (1973) or by Leung (1976).

<div align="center">

APPENDIX B
RADIATIVE TRANSFER SOLUTION FOR A COMPOSITE SHELL

</div>

Figure 7 shows that there are two (density-contrast) shells existing along the impact parameter p. We consider as many cross sections as the number of grids in the sky plane. As shown in Figure 7, the rays are chosen parallel to the line of sight (the observer sees the sphere from the X-axis direction). In our model calculation, rays are not chosen according to the tangential point of each radial shell but according to grid points. Since we are going to divide the sky plane around the nebula into small rectangular areas, parallel rays (= various impact parameters parallel to the chosen line of sight) in the nebular spherical geometry can be determined by each small grid on the plane. Therefore, if we describe the sky plane as a coordinate (y, z) from the center $(0, 0)$, the impact parameter will be given as $p = (y^2 + z^2)^{1/2}$, and we also employ the Feautrier method with a little modification.
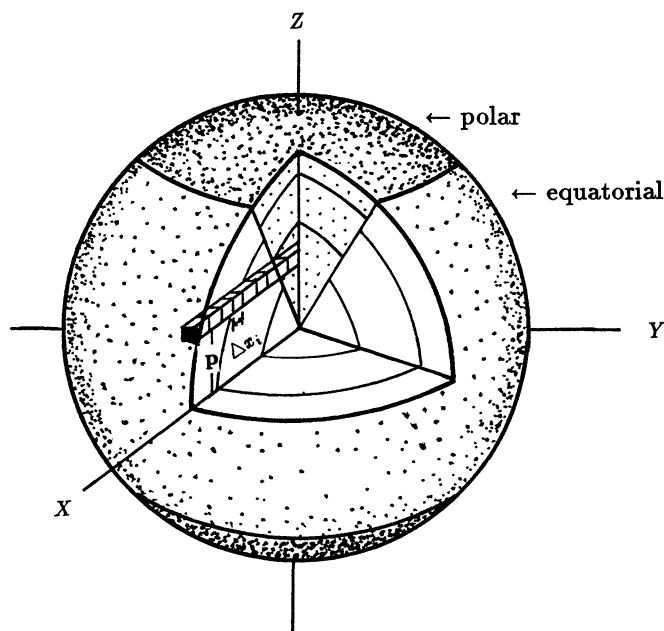
FIG. 7.—Column of "bricks" passing through a line of sight at p; the optical path length Δx_i of a brick depends on the radial distance r and the impact parameter p. This is an idealized situation where the observer is looking along an axis of symmetry ("pole of nebula" line is perpendicular to the X-axis).

The first boundary condition at the outer surface of the nebular sphere is still valid in this composite geometry (e.g., eqs. [A6] and [A7]). However, we cannot set the inner boundary condition geometrically at $x = 0$ to solve the radiative equation for the spherically nonsymmetrical geometry as shown in Figure 8. Nonetheless, the inner boundary condition for the differential equation should be found at a point which satisfies the condition $I^-(p, \tau) = I^+(p, \tau)$. Although $I^-(p, \tau) = I^+(p, \tau)$ does not occur at the middle position ($x = 0$), we may able to find this particular point x_c ($\neq 0$) from a simple numerical test. If such a point is determined, we can set the second boundary condition at $x = x_c$,

$$dU(p, \tau)/d\tau = 0, \qquad \tau = \tau_c(p) . \tag{B1}$$
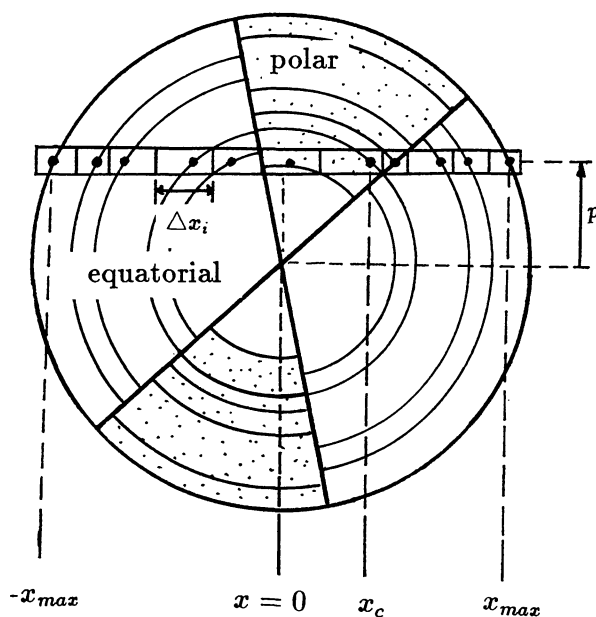
FIG. 8.—Cross section containing a column of "bricks" passing through a line of sight at p. The middle point ($x = 0$) does not satisfy the condition $I^- = I^+$; however, the point ($x = x_c$) that does satisfy the $I^- = I^+$ condition must exist in the same column of "bricks."

Here $\tau_c(p)$ at x_c is not necessarily equal to $\tau_{max}(p)/2$, because the radiative transfer solutions depend on the detailed physical gaseous state of two different density regions. As one way of guessing the point $i = c$ where $I^-(p, \tau) = I^+(p, \tau)$ or $V(p, \tau) = 0$, we may use the following numerical summation of the source function $S_i|_p$ along the impact parameter p (from each local intensity $I_i = \int_0^{\Delta \tau_i} j_i e^{-t} dx_i = \int_0^{\Delta \tau_i} j_i e^{-t} dt_i/\kappa = (j_i/\kappa)[1 - \exp(\Delta \tau_i)]$):

$$\sum_{i=1}^{c} S_i[1 - \exp(-T_i)]|_p = \frac{1}{2} \sum_{i=1}^{n} S_i[1 - \exp(-T_i)]|_p, \tag{B2}$$

where the newly defined optical depth $T_i = (h_{i+1} + h_i)/2$ for $i = 2, \ldots, n - 1$, with $T_1 = h_1/2$ and $T_n = h_n/2$, and $h_k = h_k(p) = \tau_k(p) - \tau_{k-1}(p)$ also can be determined by the trapezoidal rule.

Using the second-order difference operator to replace the second derivative in equation (A5), Hummer et al. (1973) find a spline formula for U_i along the parallel rays (p) in terms of the source function S_i and the optical depth interval h_i, that is,

$$U_{i-1}(h_{i+1} - \tfrac{1}{6}h_i^2 h_{i+1}) - U_i[h_i + h_{i+1} + \tfrac{1}{3}h_i h_{i+1}(h_i + h_{i+1})] + U_{i+1}(h_i - \tfrac{1}{6}h_i h_{i+1}^2) = \tfrac{1}{6}h_i h_{i+1}[h_i S_{i-1} + 2(h_i + h_{i+1})S_i + h_{i+1}S_{i+1}]. \tag{B3}$$

With a linear equation for the first derivative (not described in detail here), we can also obtain three formulae for the boundary conditions

$$U_1(2h_2^2 + 6h_2 + 6) + U_2(h_2^2 - 6) = h_2^2(S_2 + 2S_1) \qquad \text{at } \tau = \tau_1 = 0, \tag{B4}$$

$$U_{n-1}(h_n^2 - 6) + U_n(2h_n^2 + 6h_n + 6) = h_n^2(2S_n + S_{n-1}) + 6Qh_n \qquad \text{at } \tau = \tau_n = \tau_{max} = 2\tau_m, \tag{B5}$$

and

$$-U_c(2h_{c+1}^2 + 6 + 6h_{c+1}) + U_{c+1}(6 - h_{c+1}^2) = -h_{c+1}^2(2S_c + S_{c+1}) - 6h_{c+1}Q^* \qquad \text{at } \tau = \tau_c = \tau_m. \tag{B6}$$

Q and Q^* are due to source functions other than the diffuse radiation, i.e., $Q^* = 0$, $R \le R_c$ for a hollow core (our case), or $Q^* \ne 0$, $R \le R_c$ for an opaque core. The discontinuity due to the two shell boundaries are treated in such a way that all the radiative contribution from the other shell is obtained by employing the first-order radiative equation (B2) and is considered as Q in the above spline formula (at the boundary). If the solution from the above spline formulae is not satisfactory for $i = c$, another trial is necessary with the other choices, such as $i = c - 1$ or $i = c + 1$.

As indicated by Hummer et al. (1973), the success of the procedure in this second-order radiative solution depends on the selection of the spatial grid (choice of small steps h_i). Since the radial step size is already fixed according to the main model calculation, we cannot purposely set the spatial grids to certain intervals in order to handle optical depth increments. Therefore, when the spline representation becomes unstable (the error of this spline formula is order of h_i^2; Hummer et al. 1973), it gives inadequate solutions of U and V in many cases. Near the boundaries, where the optical depths increase suddenly due to the weakness of the remaining stellar radiation field and accordingly the large optical depths, intermediate points can be added to make the value of h_i (or $\delta \tau_i$) much less than unity in the most opaque part.

In the case where the negative or other improper solutions (i.e., $U \le 0$ or $V \ge U$) are not avoidable, the straightforward first-order radiative transfer solutions for the U-values along the impact parameter p can be replaced; when the total optical length along the impact parameter p is τ_θ, the solution for equation (A4) in one direction is $I(\theta) = S_\nu(1 - e^{-\tau_\theta})$. The forward solutions for $i = 1, 2, \ldots, m$ at each spatial grid along p are repeatedly solved by using the following:

$$I_1^+ = S_1(1 - e^{-\delta h_1}),$$

$$I_2^+ = (S_1 e^{-(\delta h_2 + \delta h_1)} + S_2)(1 - e^{-\delta h_2}),$$

$$\vdots$$

$$I_m^+ = (S_1 e^{-(\delta h_m + \ldots + \delta h_2 + \delta h_1)} + \ldots + S_m)(1 - e^{-\delta h_m}), \tag{B7}$$

and similarly the backward solutions for $k' = 1, 2, \ldots, m$ are

$$I_1^b = S_1^b[1 - \exp(-\delta h_1^b)],$$

$$I_2^b = \{S_1^b \exp[-(\delta h_2^b + \delta h_1^b)] + S_2^b\}[1 - \exp(-\delta h_2^b)],$$

$$\vdots$$

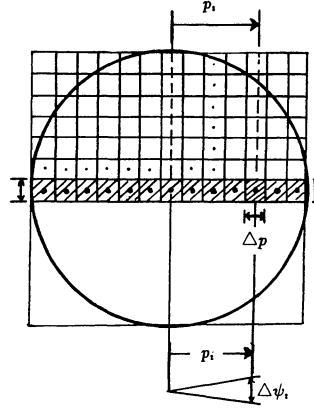$$I_m^b = (S_1^b e^{-(\cdots)} + \ldots + S_m^b)[1 - \exp(-\delta h_m^b)], \tag{B8}$$
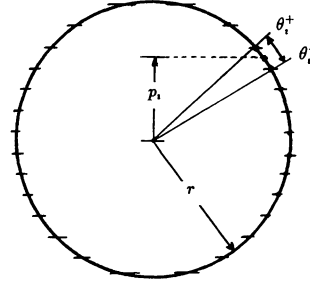
FIG. 9a   FIG. 9b

FIG. 9.—Angular quadrature weight from a small angular surface area on a radial shell r surface. (a) Various small angular surface areas on the surface of the radial shell r (to avoid any confusion, $\Delta\psi_i$ of an angular surface i is drawn at the bottom); $\Delta\psi_i \simeq 2\tan^{-1}[(\Delta p/2)/p_i]$ in the (y, z)-plane. (b) A great circle of r passing through the line of sight at p_i ($z = 0$); $\Delta\mu_i \simeq \mu_i^+ - \mu_i^- = \cos\theta_i^+ - \cos\theta_i^-$.

where $\delta h_i = (h_i + h_{i+1})/2$, $h_{k'}^b = h_{m+2-i}$, and $S_{k'}^b = S_{m+1-i}$, and $I_{k'}^b = I_{m+1-i}^-$. Finally, we find a complete set of solutions, i.e., $U_i = (I_i^+ + I_i^-)/2$, for all grids in our composite model regardless of numerous impact parameters.

Now these radiative transfer solutions should be stored separately in each radial shell of models I and II, which are to be applied again in the next iteration of the nebula program to replace the previous radiative transfer (RT) solution (where the transfer problem between shells I and II was not considered). We can now recalculate the ionization structure. Thus, the moment integral in equation (A2) should be found separately for the equatorial radial shells (I) and the polar radial shells (II), respectively.

As mentioned in the previous section, the integration of equation (A11) is to be done in the intervals between $a = 0$ and $b = 1$, if the model nebula consists of geometrically homogeneous spherical shells. In the composite model, the same procedure cannot be applied to the moment integral, so the value of a and b in equation (A11) depends on each model radius and other geometrical factors; the formulae for finding the angular quadrature weights by Leung (1976) cannot be applied in our composite model, and we therefore need to find a way to get angular quadrature weights.

The impact parameter, which is the distance from the center of the nebula to the considered points on the sky, can be evaluated as $p_j = (y_n^2 + z_{n'}^2)^{1/2} = [(n\Delta p)^2 + (n'\Delta p)^2]^{1/2}$ for $n \times n'$ grids in the (y, z)-plane. For a shell surface of radius r, there are many impact parameters passing through points on the surface (and, correspondingly, solutions U_i are given there). Since each radiative solution U_i on the sphere represents a fractional small surface area, we need to evaluate the angular quadrature weight.

Figure 9 shows the sphere of radius r, and the impact parameters that pass through each tiny area ($\Delta p \times \Delta p$) in the line-of-sight direction (x). From the various impact parameters (p_i) and the grid interval ($\Delta p/2$) as shown in Figure 9b, the angular quadrature weight can be evaluated in the following way:

$$\Delta\mu_i = \mu_i^+ - \mu_i^- = \cos\theta_i^+ - \cos\theta_i^- \ , \tag{B9}$$

where $\theta_i^\pm \simeq \sin^{-1}[(p_i \pm \Delta p/2)/r]$. Since $0 < \theta_i^\pm < \pi/2$, the restrictions $\theta_i^+ = \pi/2$ for $(p_i + \Delta p/2) > r$ and $\theta_i^- = 0$ for $(p_i - \Delta p/2) < 0$ should be given.

For a spherically symmetrical nebular model case, the U_i in equation (A11) for p_i on a cross section, which is obtained by an approximation in cylindrical coordinates, can represent the solutions for the whole nebula. However, the moment integral for a nonspherical case cannot be solved using equation (A11), because it is not symmetric through the angle ψ [i.e., $\int_0^{4\pi} dw\, I_\nu(r, \mu, \psi)/4\pi \neq \int_{-1}^{1} d\mu\, \mu^i I_\nu(r, \mu)/\int_{-1}^{1} d\mu$ in eq. (A2)]. Thus, the moment integral should be further weighted by the other angular weight $\Delta\psi_j$. In the non–spherically symmetric nebular model, the solution for the U_i is responsible for each fractional volume element. Therefore, we use the following relation, which is basically determined from each angular area of the grid (Fig. 9a) in the (y, z)-plane,

$$\Delta\psi_j \simeq 2\tan^{-1}\left(\frac{\Delta p/2}{p_j}\right), \tag{B10}$$

with $\Delta\psi_j = 2\pi$ for $p_j = 0$ (i.e., when passing through the central point).

REFERENCES

Adam, J., & Köppen, J. 1985, A&A, 142, 461
Aller, L. H. 1984, Physics of Thermal Gaseous Nebulae (Dordrecht: Reidel)
Aller, L. H. 1987, in Spectroscopy of Astrophysical Plasmas, ed. A. Dalgarno & D. Layzer (Cambridge Astrophysics Series; Cambridge: Cambridge Univ. Press), 113

Aller, L. H. 1990, PASP, 102, 1097
Aller, L. H., Baker, J. G., & Mendez, R. H. 1939a, ApJ, 89, 587
———. 1939b, ApJ, 90, 601
Aller, L. H., & Czyzak, S. J. 1979, Ap&SS, 62, 397
———. 1983, ApJS, 51, 211
Aller, L. H., & Keyes, C. D. 1987, ApJS, 65, 405
Aller, L. H., Keyes, C. D., Maran, S. P., Gull, T. Michalitsianos, A. G., & Stecher, T. P. 1987, ApJ, 320, 159
Aller, L. H., & Liller, W. 1968, in Stars and Stellar Systems, Vol. 7, Nebulae and Interstellar Matter, ed. B. M. Middlehurst & L. H. Aller (Chicago: Univ. Chicago Press), Plate 7
Baker, J. G., Aller, L. H., & Mendez, R. H. 1939, ApJ, 90, 271
Baker, J. G., Mendez, R. H., & Aller, L. H. 1938, ApJ, 88, 422
Balick, B. 1975, ApJ, 201, 705
———. 1987, AJ, 94, 671
Barker, T. 1983, ApJ, 267, 630
Barlow, M. J. 1983, in IAU Symp. 103, Planetary Nebulae, ed. D. R. Flower (Dordrecht: Reidel), 105
Butler, K., & Zeippen, C. J. 1989, A&A, 208, 337
Clegg, R. E. S. 1987, MNRAS, 229, 31P
Clegg, R. E. S., & Harrington, J. P. 1989, MNRAS, 239, 869
Clegg, R. E. S., Harrington, J. P., Barlow, M. J., & Walsh, J. R. 1987, ApJ, 314, 551
Clegg, R. E. S., & Middlemass, D. 1987, MNRAS, 228, 759
Code, A. D. 1960, in Stars and Stellar Systems, Vol. 6, Stellar Atmospheres, ed. J. L. Greenstein (Chicago: Univ. Chicago Press), 50
Daub, C. T. 1982, ApJ, 260, 612
Dopita, M. A., & Meatheringham, S. J. 1990, ApJ, 357, 140
Draine, B. T., & Lee, H. M. 1984, ApJ, 285, 89
———. 1987, ApJ, 318, 485
Harrington, J. P. 1967, Ph.D. thesis, Ohio State Univ.
———. 1983, in IAU Symp. 103, Planetary Nebulae, ed. D. R. Flower (Dordrecht: Reidel), 219
———. 1989, in IAU Symp. 131, Planetary Nebulae, ed. S. Torres-Peimbert (Dordrecht: Kluwer), 157
———. 1991, private communication
Harrington, J. P., & Feibelman, W. A. 1983, ApJ, 265, 258
Harrington, J. P., Lutz, J. H., & Seaton, M. J. 1981, MNRAS, 195, 21
Harrington, J. P., & Marionni, P. A. 1976, ApJ, 206, 458
Harrington, J. P., Monk, D. J., & Clegg, R. E. S. 1988, MNRAS, 231, 577
Harrington, J. P., Seaton, M. J., Adams, S., & Lutz, J. H. 1982, MNRAS, 199, 517
Hayes, D. S. 1970, ApJ, 159, 165
Hayes, D. S., & Latham, D. W. 1975, ApJ, 197, 593
Heap, S. R., Corcoran, M., Hintzen, P., & Smith, E. 1991, NASA/Goddard Space Flight Center preprint
Hua, C. T., & Grundseth, B. 1985, AJ, 90, 2055
Hubeny, I. 1988, Comput. Phys. Comm., 52, 103
———. 1992, private communication

Hummer, D. G., & Kunasz, P. B. 1980, ApJ, 236, 609
Hummer, D. G., Kunasz, C. V., & Kunasz, P. B. 1973, Comput. Phys. Comm., 6, 38
Hummer, D. G., & Seaton, M. J. 1963, MNRAS, 127, 217
Hummer, D. G., & Storey, P. J. 1987, MNRAS, 224, 801
Hyung, S. 1992, Ph.D. thesis, Univ. California, Los Angeles
IAU Symp. 155. 1992, Planetary Nebulae (Dordrecht: Kluwer), in press
Icke, V., Balick, B., & Frank, A. 1992, A&A, 253, 224
Jacoby, G. H., & Ford, H. C. 1988, ApJ, 266, 298
Kaler, J. B., Czyzak, S. J., & Aller, L. H. 1968, ApJ, 153, 43 (KCA)
Keyes, C. D., & Aller, L. H. 1978, Ap&SS, 59, 91
Keyes, C. D., Aller, L. H., & Feibelman, W. A. 1990, PASP, 102, 59
Kwok, S. 1982, ApJ, 258, 280
Kwok, S., Purton, C. R., & FitzGerald, M. P. 1978, ApJ, 219, L125
Latham, D. W., & Sternberg, A. 1977, CfA Preprint 827
Leung, C. M. 1976, J. Quant. Spectrosc. Rad. Transf., 16, 559
Maciel, W. 1985, Rev. Mexicana Astron. Af., 10, 199
Marionni, P. A., & Harrington, J. P. 1981, in The Universe at Ultraviolet Wavelengths, ed. R. D. Chapman (NASA CP-2171), 633
Masson, C. R. 1989, ApJ, 346, 243
Mathis, J. S. 1990, ARA&A, 28, 37
Mathis, J. S., Rumpl, W., & Nordsieck, K. H. 1977, ApJ, 217, 425
Mellema, G., Eulderink, F., & Icke, V. 1991, A&A, 252, 718
Mendez, R. H., Kudritzki, R. P. Herrero, A., Husfeld, D., & Groth, H. G. 1988, A&A, 190, 113
Mendoza, C. 1983, in IAU Symp. 103, Planetary Nebulae, ed. D. R. Flower (Dordrecht: Reidel), 143
Menzel, D. H., & Aller, L. H. 1941, ApJ, 94, 30
Menzel, D. H., Aller, L. H., & Baker, J. G. 1938, ApJ, 88, 313
National Optical Astronomy Observatories. 1987, IRAF User Handbook
Nuth, J. A. 1985, Nature, 318, 166
Osterbrock, D. E. 1989, Astrophysics of Gaseous Nebulae and Active Galactic Nuclei (Mill Valley: University Science Books)
Palmer, B. A., & Engeleman, J. R. 1983, Atlas of the Thorium Spectrum (Los Alamos National Laboratory)
Péquignot, D. 1983, in IAU Symp. 103, Planetary Nebulae, ed. D. R. Flower (Dordrecht: Reidel), 173
Pottasch, S. R., Gross, W. M., Arnal, E. M., & Gathier, R. 1982, A&A, 106, 229
Rawlings, J. M. C., & Williams, D. A. 1989, MNRAS, 240, 729
Seaton, M. J. 1979, MNRAS, 187, 73P
Spitzer, L. 1948, ApJ, 107, 6
Stephens, J. R. 1980, ApJ, 237, 450
Torres-Peimbert, S., & Peimbert, M. 1977, Rev. Mexicana Astron. Af., 2, 181 (TPP)
Tylenda, R. 1979, Acta Astron., 29, 355
Wright, E. L. 1987, ApJ, 320, 818
Zanstra, H. 1931, Pub. Dom. Ap. Obs., 4, 209
Zeippen, C. J., Butler, K., & Le Bourlot, J. 1987, A&A, 188, 251